1 **REVISION 2**

2 **Spectroscopic study on the local structure of sulfate (SO_4^{2-}) incorporated in**
3 **scorodite ($FeAsO_4 \cdot 2H_2O$) lattice: Implication for understanding the Fe(III)-**
4 **As(V)-SO_4^{2-} bearing minerals formation**

5 XU MA[1], FENGDAI QI[1], MARIO ALBERTO GOMEZ[3], RUI SU[2], ZELONG YAN[1],
6 SHUHUA YAO[3], SHAOFENG WANG[2,] *, YONGFENG JIA[2]
7 [1] Key Laboratory of Industrial Ecology and Environmental Engineering (Ministry of
8 Education, China), School of Environmental Science and Technology, Dalian
9 University of Technology, Dalian 116024, China.
10 [2] Institute of Applied Ecology, Chinese Academy of Sciences, Shenyang 110016,
11 China.
12 [3] Liaoning Engineering Research Center for Treatment and Recycling of Industrially
13 Discharged Heavy Metals, Shenyang University of Chemical Technology, Shenyang
14 110142, China.
15 * Corresponding authors: Telephone: +86 24 83970502
16 E-mail addresses: wangshaofeng@iae.ac.cn (Shaofeng Wang).
17

ABSTRACT

The incorporation of sulfate (SO_4^{2-}) into the scorodite ($FeAsO_4 \cdot 2H_2O$) lattice is an important mechanism during arsenic (As) fixation in natural and engineered settings. However, spectroscopic evidence of SO_4^{2-} speciation and local structure in scorodite lattice is still lacking. In this study, X-ray diffraction (XRD), Fourier transform infrared spectroscopy (FTIR), sulfur *K*-edge X-ray absorption near edge structure (XANES), and extended X-ray absorption fine structure (EXAFS) spectroscopic analyses in combination with density functional theory (DFT) calculations were used to determine the local coordination environment of SO_4^{2-} in the naturally and hydrothermally synthetic scorodite. The natural scorodite on SO_4^{2-} retention and the effect of pH value and initial Na^+ concentration on the incorporation of SO_4^{2-} in synthetic scorodite were investigated. The results showed that trace amounts of SO_4^{2-} were incorporated in natural scorodite sample. Scanning electron microscopy (SEM) results revealed that SO_4^{2-} was homogeneously distributed inside the natural and synthetic scorodite particles, and its content in the synthetic scorodite increased slightly with initial Na^+ concentration at pH of 1.2 and 1.8. The FTIR features and XANES results indicated that the coordination number (CN) of FeO_6 octahedra around SO_4^{2-} in scorodite lattice is four. The DFT calculation optimized interatomic distances of S-O were 1.45, 1.46, 1.48, and 1.48 Å with an average of ~1.47 Å, and the interatomic distances of S-Fe were 3.29, 3.29, 3.33, and 3.41 Å with an average of ~3.33 Å. EXAFS analysis gave an average S-O bond length of 1.47(1), and S-Fe bond length of 3.33(1) Å with a $CN_{S\text{-}Fe}$=4 for SO_4^{2-} in the scorodite structure, in good agreement with the DFT optimized

structure. The results conclusively showed that SO_4^{2-} in the scorodite lattice may be in the form of a $Fe_2(SO_4)_3$-like local structure. The present study is significant for understanding the formation mechanism of scorodite in natural environments and hydrometallurgical unit operations for waste sulfuric acid treatment.

Keywords: Arsenic, Scorodite, Sulfate, Incorporation, Local environment

INTRODUCTION

Crystalline ferric arsenate (scorodite, $FeAsO_4 \cdot 2H_2O$) is one of the least soluble As phases and a pivotal secondary As-bearing mineral controlling the fate and transport of As in acidic Fe(III)-As(V)-SO_4^{2-}-H_2O systems, such as arsenic-contaminated soil, hydrometallurgical tailings, and acid mine drainage (AMD) (Giere et al. 2003; Drahota and Filippi 2009; Murciego et al. 2011). Several studies have found that arsenopyrite (FeAsS) and arsenical-pyrite (As-FeS_2) solid wastes in abandoned mine tailings were enveloped by secondary scorodite and amorphous ferric arsenate under natural weathering conditions (Flemming et al. 2005; Langmuir et al. 2006; Paktunc and Bruggeman 2010). Furthermore, scorodite precipitation is a sink for As in metallurgical processing due to its high As content (~32 wt%), low solubility, and good-settling properties (Debekaussen et al. 2001; Fujita et al. 2008b, 2008c, 2009b; Le Berre et al. 2008; Ma et al. 2019; Zhu et al. 2019).

It is well known that scorodite can be formed in natural and industrial settings, where the dissolved Fe and As appeared simultaneously with sulfate (SO_4^{2-}). For example, the natural weathering of arsenide or sulfide minerals in natural settings (i.e., AMD), and the utilization of $Fe_2(SO_4)_3$ or $FeSO_4$ as an iron source for the conversion

of arsenic into scorodite in metallurgical plant effluents (Giere et al. 2003; Drahota and Filippi 2009; Murciego et al. 2011). It has been reported that dissolved SO_4^{2-} concentrations in such natural settings and industrial systems are a few orders of magnitude higher than those of toxic elements (e.g., As, Cu^{2+}, Zn^{2+}, Pb^{2+}, and Cd^{2+}) at a wide pH range (-3.6 to circumneutral) (Nordstrom et al. 2000; López-Archilla et al. 2001; Casiot et al. 2003; Morin et al. 2003; Maillot et al. 2013). Due to the similar geometry and charge between $HAsO_4^{2-}$ and SO_4^{2-}, $HAsO_4^{2-}$ can be incorporated into SO_4-bearing minerals via the isomorphic substitution for SO_4^{2-} and forming solid solutions. For example, As(V)-barite ($Ba(SO_4)_x(HAsO_4)_{1-x}$), As(V)-gypsum ($Ca(SO_4)_x(HAsO_4)_{1-x}\cdot 2H_2O$) and basic ferric arsenate sulfate solid solutions ($Fe(AsO_4)_{0.2-0.7}(SO_4)_{0.7-0.2}(OH)_{0.7-0.2}$) have been reported (Fernández-Martínez et al. 2008; Gomez et al. 2010; Bolanz et al. 2016; Ma et al. 2017). Analogously, coexisting SO_4^{2-} can also be incorporated into the scorodite host phase and form a SO_4-scorodite solid solution (Fujita et al. 2009b).

It is widely accepted that the Fe(III)-sulfate-bearing phase minerals originate from aqueous Fe(III)-SO_4^{2-} complexes such as $FeSO_4^+$ and $Fe(SO_4)_2^-$ (Majzlan and Myneni 2005). Therefore, the crystallization and precipitation of scorodite in the presence of Fe(III)-SO_4^{2-} complexes may be one of the main reasons for the formation of SO_4-scorodite solid solution (Majzlan and Myneni 2005; Yang et al. 2015; Chai et al. 2017). Some detailed investigations of the nucleation and crystallization of scorodite in the presence of SO_4^{2-} have been performed to explore the optimal parameters for As fixation in metallurgical plant effluents (Singhania et al. 2006; Fujita et al. 2008a;

Gomez et al. 2011; Qi et al. 2020). It has been reported that elevated aqueous SO_4^{2-} concentrations can significantly reduce the crystallinity and particle size of hydrothermally synthetic scorodite (Singhania et al. 2006). Gomez et al. (2011) found that scorodite could incorporate a considerable amount of SO_4^{2-}, which can reach up to 5.0 wt%. The incorporated structural SO_4^{2-} in the scorodite lattice can cause a decrease in its stability and increase its corresponding arsenic mobility (Fujita et al. 2009a). It has been reported that the leached As from a synthetic atmospheric scorodite using the Toxicity Characteristic Leaching Procedure (TCLP) rose from 1.9 to 2.8 mg/L with the content of incorporated SO_4^{2-} increasing from 2.5 to 4.2 wt.% (Singhania et al. 2006). Therefore, understanding the local SO_4^{2-} coordination environment has important implications for understanding the role of SO_4^{2-} in scorodite formation, structural stabilization, and reactivity. Furthermore, it can give us more insights into the transport and transformation behavior of As. Based on the fact that the isomorphic substitution between $HAsO_4^{2-}$ and SO_4^{2-} in minerals (e.g., jarosite, gypsum, and barite) occurs (Fernández-Martínez et al. 2008; Gomez et al. 2010; Bolanz et al. 2016), Fujita et al. (2009a) proposed that SO_4^{2-} was more likely incorporated into scorodite via the isomorphic substitution for AsO_4, in a formula $Fe(AsO_4)_x(SO_4)_{1-x}\cdot 2H_2O$. On the other hand, they also studied the effect of pH and solution compositions, such as divalent metal cations and Na^+ on the physical properties and stability of the hydrothermal synthetic scorodite. However, to the best of our acknowledge, the quantitative investigation of doped SO_4^{2-} and its local structure in scorodite using spectroscopic method is still lacking.

As such various analytical techniques, including X-ray diffraction (XRD), scanning electron microscopy-energy dispersive X-ray spectroscopy (SEM-EDX), Fourier transform infrared spectroscopy (FTIR), and synchrotron-based sulfur *K*-edge X-ray absorption fine spectroscopy (XAFS) were used to determine the SO_4^{2-} coordination environments in scorodite. Density functional theory (DFT) calculations were also utilized to construct the local molecular structure of SO_4^{2-} in scorodite. The objectives of the present study are (1) to quantitatively investigate the content of SO_4^{2-} incorporated into scorodite at different initial Na^+ concentrations; (2) to elucidate the local coordination environment of SO_4^{2-} in scorodite.

MATERIALS AND METHODS

Materials

Analytical grade reagents, clean glassware, and Deionized (DI) water (18.2 MΩ cm) were used for all experiments. The stock solutions of As(V), Fe(III), [Fe(II)+SO_4^{2-}], and Na^+ were prepared by dissolving As_2O_5, $Fe(NO_3)_3 \cdot 9H_2O$, $FeSO_4 \cdot 7H_2O$, and $NaNO_3$ into acidic DI-water, respectively. The varied coexisting Na^+ concentrations (ionic strength) may affect the efficiency of As precipitation. However, in this work, the evaluation of the arsenic precipitation efficiency during scorodite formation is beyond the scope of the present paper.

Natural and hydrothermally synthetic SO_4^{2-} doped scorodite samples

One natural scorodite sample (defined as *Natural-scorodite* hereafter) was collected from Guangxi, China, for the evaluation of natural scorodite on SO_4^{2-} retention in natural settings. Figure 1 shows that the natural scorodite single-crystal

particles appeared as pyramidal or pseudo-octahedral shapes with sizes up to several millimeters. The scorodite grains were enveloped by arsenical-pyrite crystals, revealing that the secondary scorodite mineral was originated from the natural weathering of arsenical-pyrite (data not shown), in agreement with the previous reports (Paktunc and Bruggeman 2010). The selected parts of *Natural-scorodite* single-crystal particles were cut or ground to obtain the cross-section or solid powders, then cleaned with 70% ethanol via ultrasound for chemical characterization.

The SO_4^{2-} doped scorodite (denoted as *SO_4-scorodite* hereafter) was synthesized at a fixed SO_4^{2-}:Fe(II):As(V) molar ratio of 1.5:1.5:1 with various initial Na^+ concentrations at pH 1.2 and 1.8 via the method previously reported by Fujita et al. (2008a). Relative high [SO_4^{2-}+Fe]/As ratio and acidity used in the present study are relevant to AMD sties and industrial operations (Debekaussen et al. 2001; Casiot et al. 2003; Fujita et al. 2009; Murciego et al. 2011; Min et al. 2015). Various initial Na^+ concentrations was used based on the fact that the ionic strength is an important parameter in AMD and waste sulfuric acid and Na^+ has negligible effect on the crystallization and transformation of scorodite. The synthesis of SO_4^{2-}-doped scorodite was performed by introducing a $FeSO_4 \cdot 7H_2O$ solution into a mixture of As(V) and Na^+ solution at 95 °C simultaneously with Fe(II) oxidization via air bubbling. Briefly, 100 mL of 0.2 M As(V)+Na^+ solutions with varying concentrations of NaCl solutions (i.e., 0, 2, 4, and 8 M) were prepared by mixing As(V) and NaCl solutions. Then 100 mL $Fe^{II}SO_4$ solution was pre-adjusted to pH 1.2 or 1.8 by using 2 M HCl. This solution was then added into the As(V)+Na^+ solutions (Fe/As molar ratio =1.5) to precipitate SO_4-

scorodite under mechanical agitation and heated at 95 °C followed by slow Fe(II) oxidization via air bubbling. The volume of the final solution was ~200 mL. The final concentrations in the systems were: 0.1 M As, 0.15 M Fe, and 0.15 M SO_4^{2-} with various additional Na^+ concentrations of 0, 1, 2, and 4 M. The final suspensions were subjected to solid-liquid separation by filtration through 0.22-μm membranes. All solid samples were washed five times with 0.1 mM HCl solutions (pH ~4) to remove the residual solutions in the solids since scorodite has a relatively low degree of solubility at such pH conditions (Langmuir et al., 2006). Then the solids were freeze-dried, and stored in a desiccator for further solid characterization.

Synthesis of standard compounds

The SO_4-bearing hydrous ferric arsenate (defined as *SO_4-ferric arsenate* hereafter) was synthesized according to the method reported previously (Wang et al. 2016). Briefly, an equal volume of 0.2 M As(V) (As_2O_5) and 0.2 M Fe(III) ($Fe_2(SO_4)_3$) solutions were mixed at pH 1.2 and maintained at that pH for 24 h by using NaOH or HCl solutions. The SO_4-free scorodite (defined as *scorodite* hereafter) was synthesized using $Fe(NO_3)_3 \cdot 9H_2O$ as a Fe source by continuous heating of As(V) and Fe mixed solutions (0.15 M Fe and 0.15 M As, pH 1.2) at 95 °C for 12 h. Jarosite ($KFe_3(SO_4)_2(OH)_6$) synthesis was carried out by heating the mixture of 0.2 M Fe (from $Fe_2(SO_4)_3$) and 0.3 M SO_4^{2-} (K_2SO_4) solution at pH 1.4 and 98 °C for 24 h (Paktunc and Dutrizac 2003). All the synthetic solids were separated by centrifugation, washed five times using DI water with the same pH as the reaction systems. This was done to remove the interparticle-entrained residual solutions. The solids were then freeze-dried

and stored in a desiccator for further analysis.

Determination of SO_4^{2-} contents in scorodite

A known amount of solid samples were digested in 6 M HCl, and the clear solutions were used to analyze the SO_4^{2-} concentrations. The concentration of dissolved SO_4^{2-} in solution was determined by the nephelometric method using a UV-visible spectrophotometer (Shimadzu, Japan) at 420 nm. The detection limit for SO_4^{2-} was 0.1 mg/L with an uncertainty of ±5% (Sörbo 1987).

Solid-phase characterization

The mineralogical characteristics of the solid samples were determined by using a Rigaku D/max 2400 X-ray diffractometer (Rigaku Corporation, Japan) equipped with a copper target (Cu$K\alpha_1$ radiation, λ = 1.54056 Å), a graphite monochromator, and a scintillation detector. The equipment was run at 56 kV and 182 mA by step scanning 2θ from 10° to 80° with an increment of 0.02°. The pattern refinement in the range of 2θ 10° to 60° was executed.

The morphologies and elemental distribution of the solid samples were characterized using scanning electron microscopy coupled with energy-dispersive X-ray spectroscopy (SEM-EDX) on a scanning electron microscope (Phenom ProX, Netherlands). Two methods were used for analysis, i: placed the solid particles on double-sided carbon tape and examined them with SEM-EDX; ii: mounted the solid particles in a cold setting epoxy resin, which once solidified was polished to uncover the particles from the resin and create cross-sections of the particles for point element mapping analysis.

Fourier transform infrared spectroscopy (FTIR) of the solid samples were collected on a Thermo Nicolet 6700 Fourier transform infrared spectrometer. Approximately 5 mg was mixed with 200 mg high purity KBr and then pressed into a disk. The spectra were collected in the range of 400 - 4000 cm^{-1} with a spectral resolution of 4 cm^{-1} and 128 co-added scans in transmission mode.

The sulfur (S) *K*-edge X-ray absorption fine spectra (XAFS) was collected on the 4B7A-mid-energy station at the Beijing Synchrotron Radiation Facility (BSRF) to determine the SO_4^{2-} coordination environments in *SO_4-scorodite*. The storage ring was operated at 2.5 GeV and 250 mA. The measurements were carried out at ambient temperature under high vacuum (10^{-6} - 10^{-8} mbar) conditions in fluorescence mode. Each spectrum was collected between -50 eV and 750 eV before and after the S *K*-edge absorption edge (~2482 eV). The step size was set to 0.1 eV/step for the pre-edge region, 3 eV/step for the XANES region, and 3 eV/step for the EXAFS region. The XAFS spectra were Fourier transformed from k to R space using Kaiser-Bessel apodization windows with an R_{bkg} value of 0.9 Å. The k-space range was set to 4 - 11 $Å^{-1}$ to obtain the radial structural functions (RSFs). The final fitting of the spectra was made on Fourier transformed k^3 weighted spectra in R space. For data fitting and modeling, scattering paths were calculated with ATOMS and FEFF using Na_2SO_4 and paracoquimbite ($Fe_2(SO_4)_3 \cdot 9H_2O$), $Fe_2(SO_4)_3$ crystallographic data (Fang and Robinson 1970; Hawthorne and Ferguson 1975; Christidis and Rentzeperis 1976).

DFT modeling

The structure of SO_4^{2-}-doped scorodite was optimized by applying density

functional theory (DFT), using the pw.x code available in the QUANTUM ESPRESSO (v. 6.3) software package (Giannozzi 2009). The code uses plane waves and pseudopotentials to solve the Kohn-Sham equations. The geometric optimization was performed in a periodic system using the generalized gradient approximation (GGA) of the Perdew-Wang (PW91) type (Giacomazzi and Scandolo 2010), and the semi-empirical dispersion correction at the D2 level (DFT-D2) (Grimme 2006). All calculations were repeated with the GGA+*U* method (Anisimov et al. 1991), which accounts for strong correlations. Norm-conserving pseudopotentials were used for all calculations. The crystallographic data of scorodite obtained from Kitahama et al. (1975) was used as the initial model with the dimension of 8.953 × 10.325 × 10.038 $Å^3$ ($a \times b \times c$) and cell volume of 927.91 $Å^3$. The SO_4-doped scorodite was built by one SO_4OH substituting for one $AsO_4(H_2O)$ in the scorodite lattice and corresponded to a SO_4^{2-} concentration of 5.32 wt%, which was used in the initial model for EXAFS fitting. The plane-wave kinetic energy cut-off for wave functions, charge density, and potential were set as 80 Ry and 320 Ry, respectively. Tests showed that these parameters could give a satisfactory convergence of total energy (< 0.2 mRy/atom).

RESULTS AND DISCUSSION

Contents of SO_4^{2-} in natural and hydrothermally synthetic scorodite

The chemical composition of the single-crystal of *Natural-scorodite* is tested (Table S1). The results showed that Fe(III) and As(V) content in *Natural-scorodite* samples were up to 22.6 wt.% and 30.5 wt.%, respectively, nearly consistent with the content of Fe and As in the scorodite standard that was 24.2 wt.% and 32.4 wt.%. The

content of SO_4^{2-} was 2.87 wt% in *Natural-scorodite*. According to the contents of Fe, As, S, and divalent metal cations, i.e. Cu^{2+}, Pb^{2+}, and Cd^{2+} (Table S1) in *Natural-scorodite* and the molecular charge balance principle, the molecular formula of *Natural-scorodite* could be described by $Fe_{0.94}(AsO_4)_{0.9}(SO_4)_{0.1}Me_{0.06} \cdot 2H_2O$, where Me represents divalent metals. Based on the charge balance principle and stoichiometry of Fe, As, SO_4^{2-}, and Me(II)s in *Natural-scorodite*: ($3 \times Fe^{3+} + 2 \times Me(II) = 3 \times AsO_4^{3-} + 2 \times SO_4^{2-}$), we extrapolated that approximately 40% SO_4^{2-} is associated with Fe^{3+}, while the other 60% SO_4^{2-} may be balanced with Me(II)s and trapped in scorodite host phase via the incorporation or solid inclusions of $MeSO_4$. To avoid the impurities-effect and better evaluate the local structure of SO_4^{2-} in scorodite lattice, the synthetic scorodite in lab-scale was performed to investigate the local coordination environments of SO_4^{2-} in scorodite, as shown below.

Figure 2 shows the contents of SO_4^{2-} in scorodite as a function of Na^+ concentration at pH 1.2 and 1.8. The results showed that the contents of SO_4^{2-} in scorodite decreased slightly from 3.66 to 1.93 wt% and 3.87 to 2.15 wt% with increasing Na^+ concentrations from 0 to 4 M at pH 1.2 and 1.8. This result suggests that the amount of incorporated SO_4^{2-} in scorodite decreased slightly with increasing initial Na^+ concentrations, in agreement with the observation of Fujita et al. (2009a) (Figure S1). It is worth to note that $FeSO_4^+$ and $Fe(SO_4)_2^-$ are the precursor for the formation of *SO_4-scorodite* (Majzlan and Myneni 2005). The decreased structural SO_4 contents could be ascribed to the increased percentage of $NaSO_4^-$ complex in terms of total S with increasing Na^+ concentrations ($Na^+ + SO_4^{2-} = NaSO_4^-$, $\log K_{sp} = 0.936$, Table S2).

This reduces the effective concentrations of Fe(III)-SO_4^{2-} complexes and SO_4^{2-} for *SO_4-scorodite* formation. Furthermore, the amount of incorporated SO_4^{2-} at pH 1.8 was slightly higher than at pH 1.2 with the same initial Na^+ concentration, possibly due to slightly higher percentage of [$FeSO_4^+$ + $Fe(SO_4)_2^-$] complexes formed at pH 1.8 *vs*. 1.2 (Table S2 and Figure S2). Previous studies have reported that the solution stability of scorodite decreases with increasing the incorporated amounts of SO_4^{2-}. Hence, the following sections of this study focused on the determination of sulfate coordination environment in scorodite.

Mineralogical results

The mineralogical characteristics of *Natural-scorodite* and *SO_4-scorodite* synthesized at various initial Na^+ concentrations were characterized by XRD and compared with reference compounds (*SO_4-ferric arsenate* and *scorodite*) (Figure 3). As can be seen, the *SO_4-ferric arsenate* showed two broad humps at 2θ of ~28.52° and ~60.24°, indicating its amorphous nature. In comparison, the main XRD peaks of *Natural-scorodite*, the synthesized *scorodite* and *SO_4-scorodite* are almost located at the same positions, hence indicating the dominant crystalline phase was scorodite. This result also suggests that the incorporation of SO_4^{2-} did not modify the characteristic structure of scorodite. However, the incorporation of SO_4 slightly altered the lattic parameters of scorodite (Figure S3). In the case of *scorodite*, the diffraction peaks of the (212), (131), (133) planes located at 2θ of ~28.16°, 29.28°, 29.88° were observed. However, in the SO_4^{2-} incorporated samples, the same diffraction peaks shifted to ~28.06°, 29.16°, and 29.76°. The refinements showed that the incorporation of SO_4^{2-}

into the structure of scorodite induced a slight volume decrease of its unit cell (Table S3). This result suggests that the incorporation of SO_4^{2-} distorts the scorodite lattice slightly. For the XRD patterns of *Natural-scorodite*, we did not perform the refinement step because the trapped impurities in *Natural-scorodite*, i.e., Me(II) may affect the refinement results.

SEM and EDX analyses

The SEM images, elemental mapping, EDX results of *SO_4-scorodite* formed at pH 1.2 with different initial Na^+ concentrations are shown in Figure 4. It can be generally observed that the morphology of the *SO_4-scorodite* was highly dependent on the initial Na^+ concentrations. For example, *SO_4-scorodite* formed in the absence of Na^+ appeared as the aggregation of fine particles. In contrast, *SO_4-scorodite* formed in the presence of Na^+ appeared as regular orthorhombic particles with sizes of ~15 μm, regardless of the Na^+ concentration. Chemical composition analysis indicated that the SO_4^{2-} content in scorodite decreased with increasing Na^+ concentrations. These results suggested that the coexistence of Na^+ may favor the formation of the single-crystal scorodite via the inhibition of SO_4^{2-} incorporation. The elemental mapping and EDX results (Figure 4) revealed that the major elements (As, Fe, O, and S) were homogeneously distributed on the *SO_4-scorodite* particles and corresponded well with the shape of the particles examined by SEM. This result further confirms that SO_4^{2-} is trapped into the scorodite host phase, in line with the chemical composition results.

However, the above-mentioned elemental mapping and EDX analysis may only identify the elements on the surface of the *SO_4-scorodite* particles due to its limited

304 penetration depth. Hence, in order to clearly show that SO_4^{2-} may have been
305 incorporated into the scorodite lattice, cross-sections of *Natural-scorodite* and *SO_4-*
306 *scorodite* particles formed at various initial Na^+ concentrations were analyzed by
307 elemental mapping (Figure 5). It can be seen that elements O, As, Fe, and S showed a
308 clear boundary between the cross-section part and epoxy resin part, while the S revealed
309 a heterogeneous distribution. This result confirmed that SO_4^{2-} was at least in part
310 incorporated into the scorodite host phase, consistent with the chemical composition
311 result.

312 **FTIR analysis**

313 The *SO_4-scorodite*, *Natural-scorodite*, and reference compounds were
314 characterized using FTIR spectroscopy (Figure 6). The frequency regions of interest
315 (400 - 1300 cm^{-1} and 2000 - 4000 cm^{-1}, Figure 6a) are the infrared active stretching and
316 bending vibrations of SO_4, AsO_4 and H_2O/OH (Omori 1968; Myneni et al. 1998). The
317 IR band positions of the stretching and bending vibrations of SO_4 in the reference
318 compounds and *SO_4-scorodite* are tabulated in Table 1. For the SO_4-ferric arsenate
319 (Figure 6b), three weak broad bands at ~1066, 1124, and 1187 cm^{-1} were ascribed to
320 the v_3 stretching vibrations of SO_4 (Hug 1997; Peak et al. 1999; Lane 2007); no band
321 was observed in this region for pure ferric arsenate and scorodite. In contrast, *SO_4-*
322 *scorodite* showed one SO_4 v_1 stretching vibration at ~1001 cm^{-1} and three SO_4 v_3
323 stretching vibrations at ~1070, 1103, and 1205 cm^{-1} (Table 1 and Figure 6). The results
324 indicated that the SO_4 vibrational modes in scorodite were significantly different from
325 those of $NaSO_4$, SO_4-ferric arsenate, paracoquimbite, and jarosite, suggesting that a

different coordination environment SO_4^{2-} may exist in the *SO_4-scorodite*.

The relationship between the symmetry of SO_4 in minerals and their infrared spectra has been well established based on infrared theory (Peak et al. 1999). The SO_4 coordination environments in reference compounds (römerite, paracoquimbite, jarosite, and $FeOHSO_4$) are shown in Figure S4. For structural SO_4 that had similar bonding environments, such as $NaSO_4$ and $FeOHSO_4$ with an S-Fe coordination number (CN) of 0 and 4 (Figure S4), which corresponding to the site symmetry of C_1 (Table 1). As such they exhibited one v_1 band for Na_2SO_4 and [one v_1 band and three v_3 bands] for $FeOHSO_4$. For römerite with $CN_{S\text{-}Fe}$=1, the symmetry of monodentate SO_4 will be lowered to C_{3v}, causing the split of ν_3 into two bands with one infrared active v_1 band (Table 1). For paracoquimbite ($CN_{S\text{-}Fe}$=2), the bidentate complex structure will further lower the symmetry of SO_4^{2-} to C_{2v} with the v_3 band splitting into three bands in the frequency range of 1050 - 1250 cm^{-1} (Hug 1997; Peak et al. 1999) (Table 1). Based on this theory, the one v_1 and three v_3 stretching vibration bands indicated that structural SO_4^{2-} in *SO_4-scorodite* was associated with four Fe atoms via bridging oxygen.

XANES analysis

Figure 7 compares the S *K*-edge XANES spectra and pre-edge feature of *SO_4-scorodite* and reference compounds (Na_2SO_4 and *SO_4-ferric arsenate*). The results showed that the white line (peak B) of *SO_4-scorodit*e, *SO_4-ferric arsenate*, and Na_2SO_4 appeared at the same energy position of ~2482.5 eV, indicating the same sulfur (S) oxidation state (Figure 7a). A broad peak (peak C) in the range of (2490 - 2510 eV) above the absorption edge of Na_2SO_4 and *SO_4-scorodite* corresponded to the $1s \rightarrow$

continuum-state transition (Figure 7a). As can be seen, when SO_4 is associated with Fe(III) in the scorodite lattice, this peak C significantly shifts to higher energies in comparison with Na_2SO_4 (Myneni 2000). Additional weak pre-edge features (peak A) appeared at ~2.0 eV below the absorption edge spectra of *SO_4-scorodite* and *SO_4-ferric arsenate* samples, whereas no pre-edge feature was observed for the Na_2SO_4. These pre-edge features are caused by the electronic transition from S 1*s* orbital to 3*p* orbital that is hybridized with Fe(III) 3*d* orbitals. This pre-edge feature indicates that there exists inner-sphere bonding between SO_4^{2-} and Fe^{3+} via bridging oxygen (Okude et al. 1999; Myneni 2000; Majzlan and Myneni 2005). The increase in the number of Fe(III) atoms coordinating with SO_4^{2-} can result in the pre-edge features shifting to higher energy (Majzlan and Myneni 2005). Using this indicator, it has been proposed that each SO_4^{2-} ion complexes to one Fe^{3+} ion in an acidic SO_4-Fe(III) bearing solution (Majzlan and Myneni 2005). The pre-edge features of römerite ($Fe^{2+}Fe^{3+}_2(SO_4)_4 \cdot 14H_2O$), paracoquimbite ($Fe_2(SO_4)_3 \cdot 9H_2O$), and jarosite ($KFe^{3+}_3(SO_4)_2(OH)_6$) appeared at ~2479.4, 2479.51, and 2479.89 eV, respectively (Figure 5b and Figure S4); corresponding to the $CN_{S\text{-}Fe}$ of 1, 2, and 3 (Fanfani et al. 1970; Fang and Robinson 1970; Basciano and Peterson 2007; Gomez et al. 2013). In contrast, the pre-edge feature of *SO_4-scorodite* appeared at approximately 2480.18 eV, which was higher than those of römerite, paracoquimbite, and jarosite. This result indicates that SO_4^{2-} is more likely to coordinate with four Fe(III) atoms via bridging O. Based on this data, we can infer that SO_4 incorporates into scorodite via the isomorphic substitution for AsO_4 and is in agreement with the FTIR results.

DFT calculation

Our FTIR and XANES results suggested that each SO_4^{2-} coordinates with four Fe atoms in the *SO₄-scorodite*. Therefore, we constructed a unit crystal cell with one SO_4^{2-} substituted for one AsO_4^{3-} while controlling the charge balance to give a formula of $Fe_8(AsO_4)_7SO_4OH \cdot 15H_2O$. After which the energy minimization was performed to optimize the structure using DFT calculations as shown in Figure 8 and Figure S5. The optimized dimension was 8.8873 × 10.1919 × 9.9873 $Å^3$ (a × b × c) versus that of normal scorodite which is 8.9530 × 10.3250 × 10.0380 $Å^3$ (a × b × c), thus suggesting that the incorporation of SO_4^{2-} into scorodite reduced the volume of scorodite cell, consistent with the XRD results. The DFT optimized interatomic distances of S-O, As-O, As-Fe, and S-Fe in *SO₄-scorodite* are compared with those in $Fe_2(SO_4)_3$ and standard scorodite (Table 2). The results showed that the $d_{As\text{-}O}$ were 1.67, 1.68, 1.68, and 1.69 Å with an average of ~1.68 Å and the $d_{As\text{-}Fe}$ were 3.34, 3.35, 3.36, and 3.39 Å with an average of ~3.36 Å in scorodite. For *SO₄-scorodite*, the optimized $d_{S\text{-}O}$ were 1.46, 1.46, 1.48, and 1.48 Å with an average of ~1.47 Å, and the $d_{S\text{-}Fe}$ were 3.29, 3.29, 3.33, and 3.41 Å with an average of ~3.33 Å. The optimized interatomic distances of S-Fe were almost equal to that of $d_{S\text{-}Fe}$ in $Fe_2(SO_4)_3$ (3.30, 3.30, 3.31, and 3.31 Å) and $d_{As\text{-}Fe}$ in scorodite (Table 2). This result suggests the SO_4 local coordination environment in scorodite was similar to that of SO_4 in $Fe_2(SO_4)_3$ and as such indicates that SO_4 can substitute for the AsO_4 site in the scorodite lattice.

EXAFS analysis

EXAFS fittings were also performed to investigate the coordination environments

392 of SO_4 in our *SO_4-scorodite*. The EXAFS data of Na_2SO_4, paracoquimbite, and *SO_4-*
393 *scorodite* were fitted using the crystallographic data of $NaSO_4$, paracoquimbite, and
394 $Fe_2(SO_4)_3$ or the DFT optimized structure, respectively (Figure 9 and Table 3). In the
395 case of Na_2SO_4, the EXAFS fitting gave S-O bonds with an average interatomic
396 distance of 1.45(4) Å with a CN of 4 for the first shell, in agreement with the reported
397 crystallographic data (Hawthorne and Ferguson 1975). For paracoquimbite, the EXAFS
398 fitting gave an average S-O interatomic distance of 1.46(2) Å with a CN of 4 for the
399 first shell, and an average S-Fe interatomic distance of 3.23(5) Å with a $CN_{S\text{-}Fe}$ of 2 for
400 the second shell. This again is in agreement with the previous published
401 crystallographic data (Fang and Robinson 1970). The fewer Fe atoms binding to SO_4^{2-}
402 for the Na_2SO_4 ($CN_{S\text{-}Fe}$ =0) and paracoquimbite ($CN_{S\text{-}Fe}$ =2) than for the *SO_4-scorodite*
403 ($CN_{S\text{-}Fe}$ =4) are consistent with the lower peak intensity at ~2.9 Å (R+ΔR) in R space
404 (Figure 9b), where the S-Fe shell is located. For the *SO_4-scorodite*, the EXAFS fitting
405 showed that the first-neighbor contributions were fitted with four oxygen (O) atoms
406 with an averaged interatomic distance of 1.47(1) Å (Figure 9 and Table 3). The second
407 shell gave an average S-Fe interatomic distance of 3.33(3) Å with CN_S-Fe of
408 approximately 4, in agreement with the DFT optimized structure. Overall, the EXAFS
409 fitting results again suggested that the SO_4^{2-} may form $Fe_2(SO_4)_3$-like local structure in
410 scorodite lattice.

411 **CONCLUSIONS**

412 In this study, the effect of pH value and initial Na^+ concentration on the amount of
413 incorporated SO_4^{2-} and the local coordination environment of SO_4^{2-} in scorodite were

414 investigated by using FTIR, XANES, EXAFS spectroscopy in combination with DFT
415 calculations. The results showed that SO_4^{2-} was homogeneously distributed on the
416 scorodite host phase, and the amount of incorporated SO_4^{2-} increased slightly with
417 decreasing Na^+ concentrations or increasing pH value. The FTIR and XANES results
418 indicated that the coordination number of FeO_6 octahedra surrounding SO_4 in scorodite
419 lattice is four. The DFT modeling constructed a structure of SO_4^{2-} doped scorodite with
420 the formula of $Fe_8(AsO_4)_{15}SO_4OH{\cdot}15H_2O$ by one $SO_4(OH)$ substitution for one
421 $AsO_4(H_2O)$. The DFT optimized interatomic distances of S-O were 1.46, 1.46, 1.48,
422 and 1.48 Å with an average of ~1.47 Å, and the interatomic distances of S-Fe were 3.29,
423 3.29, 3.29, and 3.41 Å with an average of ~3.33 Å. EXAFS analysis gave an averaged
424 S-O bond lengths of 1.47(1) and an averaged S-Fe bond lengths of 3.33(3) Å with $CN_{S\text{-}Fe}$=4 for the SO_4 local environments in the scorodite lattice. This is in agreement with
426 the DFT modeling results. Overall, the spectroscopic and DFT results confirmed that
427 the SO_4^{2-} in the scorodite lattice may be in the form of a $Fe_2(SO_4)_3$-like local structure.

428 **IMPLICATIONS**

429 The transportation and evolution of Fe, As, and SO_4^{2-} and the formation of ferric
430 iron sulfate/arsenate minerals are critical geochemical processes. Among these
431 processes, the incorporation of SO_4^{2-} in the scorodite structure is an important process
432 during its formation in mining-related settings such as acid mine drainage and
433 hydrometallurgical tailings. The incorporation of SO_4^{2-} in scorodite is also an important
434 mechanism during the immobilization of arsenic in waste sulfuric acid using scorodite
435 as an As-carrier (Debekaussen et al. 2001; Fujita et al. 2008b, 2008c, 2009b; Le Berre

et al. 2008; Ma et al. 2019). The local environments of SO_4^{2-} in scorodite can provide numerous important insights into the structure, formation (i.e., grain size and surface area), and dissolution behavior of scorodite (i.e., dissolution rate). For example, the environmental stability of scorodite is controlled by its crystallinity, particle size (specific area), and structural SO_4^{2-} content. When scorodite solids have similar crystallinity and particle size, the structural SO_4^{2-} contents in scorodite may be a critical factor in controlling its stability. Our study indicated that Fe^{3+} and SO_4^{2-} may form $Fe_2(SO_4)_3$-like local structure in scorodite. Hence, we extrapolated that higher solubility of local $Fe_2(SO_4)_3$ (vs. $FeAsO_4{\cdot}2H_2O$, Table S4) trapped in scorodite may be the main reason for the higher solubility of SO_4-scorodite. Furthermore, the structure of SO_4-scorodite solid solution can also help to understand the evolution and crystallization processes of its precursors, i.e., amorphous ferric arsenate. Overall, this study is significant for understanding the speciation and formation of Fe(III)-SO_4^{2-} and Fe(III)-As(V)-SO_4^{2-} bearing minerals in natural and mining-impacted environments.

ACKNOWLEDGMENTS

We thank the National Key Research and Development Program of China (No. 2020YFC1807800), the National Natural Science Foundation of China (Nos. 41530643 and 41877393) and the Chinese Academy of Sciences (No. QYZDJ-SSW-DQC038) for the financial support. We thank the beamline 4B7A-mid-energy station at the Beijing Synchrotron Radiation Facility (BSRF) for their help on the sulfur *K*-edge XAS spectral measurements.

Appendix A. Supplementary data

Supplementary data associated with this article can be found in the online version.

Declaration of Competing Interest

The authors declare that they have no known competing financial interests or personal relationships that could have appeared to influence the work reported in this paper.

REFERENCES CITED LIST

Anisimov, V.I., Zaanen, J., and Andersen, O.K. (1991) Band theory and Mott insulators: Hubbard-U instead of Stoner I. Physical Review B, 44, 943-954.

Basciano, L.C., and Peterson, R.C. (2007) Jarosite-hydronium jarosite solid-solution series with full iron site occupancy: Mineralogy and crystal chemistry. American Mineralogist, 92, 1464-1473.

Bolanz, R.M., Gottlicher, J., Steininger, R., and Wieczorek, A. (2016) Structural incorporation of As^{5+} into rhomboclase ($(H_5O_2)Fe^{3+}(SO_4)_2{\cdot}2H_2O$) and $(H_3O)Fe(SO_4)_2$. Chemosphere, 146, 338-345.

Casiot, C., Leblanc, M., Bruneel, O., Personne, J.C., Koffi, K., and Elbazpoulichet, F. (2003) Geochemical processes controlling the formation of As-rich waters within a tailings impoundment (Carnoulès, France). Aquatic Geochemistry, 9, 273-290.

Chai, L.Y., Yang, J.Q., Zhang, N., Wu, P.J., Li, Q.Z., Wang, Q.W., Liu, H., and Yi, H.B. (2017) Structure and spectroscopic study of aqueous Fe(III)-As(V) complexes using UV-Vis, XAS and DFT-TDDFT. Chemosphere, 182, 595-604.

Christidis, P.C., and Rentzeperis, P.J. (1976) The crystal structure of rhombohedral Fe2(SO4)3. Zeitschrift Für Kristallographie, 144, 341-352.

Debekaussen, R., Droppert, D., and Demopoulos, G.P. (2001) Ambient pressure hydrometallurgical conversion of arsenic trioxide to crystalline scorodite. CIM Bulletin, 94, 116-122.

Drahota, P., and Filippi, M. (2009) Secondary arsenic minerals in the environment: A review. Environment International 35, 1243-1255.

Fanfani, L., Nunzi, A., and Zanazzi, P.F. (1970) The crystal structure of roemerite. American Mineralogist, 55, 78-89.

Fang, J.H., and Robinson, P.D. (1970) Crystal structures and mineral chemistry of hydrated ferric sulfates. I. The crystal structure of coquimbite. American Mineralogist, 55, 1534-1540.

Fernández-Martínez, A., Cuello, G.J., Johnson, M.R., Bardelli, F., Román-Ross, G., Charlet, L., and Turrillas, X. (2008) Arsenate incorporation in gypsum probed by neutron, X-ray scattering and density functional theory modeling. Journal of Physical Chemistry A, 112, 5159-5166.

Flemming, R.L., Salzsauler, K.A., Sherriff, B.L., and Sidenko, N.V. (2005) Identification of scorodite in fine-grained, high-sulfide, arsenopyrite mine-waste using micro X-ray diffraction (μXRD). Canadian Mineralogist, 43, 1243-1254.

Fujita, T., Taguchi, R., Abumiya, M., Matsumoto, M., Shibata, E., and Nakamura, T. (2008a) Effects of zinc, copper and sodium ions on ferric arsenate precipitation in a novel atmospheric scorodite process. Hydrometallurgy, 93, 30-38.

Fujita, T., Taguchi, R., Abumiya, M., Matsumoto, M., Shibata, E., and Nakamura, T. (2008b) Novel atmospheric scorodite synthesis by oxidation of ferrous sulfate

501 solution. Part I. Hydrometallurgy, 90, 92-102.

502 Fujita, T., Taguchi, R., Abumiya, M., Matsumoto, M., Shibata, E., and Nakamura, T.
503 (2008c) Novel atmospheric scorodite synthesis by oxidation of ferrous sulfate
504 solution. Part II. Effect of temperature and air. Hydrometallurgy, 90, 85-91.

505 Fujita, T., Taguchi, R., Abumiya, M., Matsumoto, M., Shibata, E., and Nakamura, T.
506 (2009a) Effect of pH on atmospheric scorodite synthesis by oxidation of ferrous
507 ions: Physical properties and stability of the scorodite. Hydrometallurgy, 96, 189-
508 198.

509 Fujita, T., Taguchi, R., Shibata, E., and Nakamura, T. (2009b) Preparation of an As(V)
510 solution for scorodite synthesis and a proposal for an integrated As fixation process
511 in a Zn refinery. Hydrometallurgy, 96, 300-312.

512 Giacomazzi, L., and Scandolo, S. (2010) Gypsum under pressure: A first-principles
513 study. Physical Review B, 81.

514 Giannozzi, P. (2009) Quantum ESPRESSO: a modular and open-source software
515 project for quantum simulations of materials. Journal of Physics Condensed Matter,
516 21, 395502.

517 Giere, R., Sidenko, N.V., and Lazareva, E.V. (2003) The role of secondary minerals in
518 controlling the migration of arsenic and metals from high-sulfide wastes (Berikul
519 gold mine, Siberia). Applied Geochemistry, 18, 1347-1359.

520 Gomez, M.A., Assaaoudi, H., Becze, L., Cutler, J.N., and Demopoulos, G.P. (2010)
521 Vibrational spectroscopy study of hydrothermally produced scorodite
522 ($FeAsO_4 \cdot 2H_2O$), ferric arsenate sub-hydrate (FAsH; $FeAsO_4 \cdot 0.75H_2O$) and basic

ferric arsenate sulfate (BFAS; $Fe(AsO_4)_{1-x}(SO_4)_x(OH)_x \cdot wH_2O$). Journal of Raman Spectroscopy, 41, 212-221.

Gomez, M.A., Becze, L., Celikin, M., and Demopoulos, G.P. (2011) The effect of copper on the precipitation of scorodite ($FeAsO_4 \cdot 2H_2O$) under hydrothermal conditions: Evidence for a hydrated copper containing ferric arsenate sulfate-short lived intermediate. Journal of Colloid and Interface Science, 360, 508-518.

Gomez, M.A., Ventruti, G., Celikin, M., Assaaoudi, H., Putz, H., Becze, L., Lee, K.E., and Demopoulos, G.P. (2013) The nature of synthetic basic ferric arsenate sulfate ($Fe(AsO_4)_{(1-x)}(SO_4)_{(x)}(OH)_{(x)}$) and basic ferric sulfate ($FeOHSO_4$): their crystallographic, molecular and electronic structure with applications in the environment and energy. RSC Advances, 3, 16840-16849.

Grimme, S. (2006) Semiempirical GGA-type density functional constructed with a long-range dispersion correction. Journal of Computational Chemistry, 27, 1787-1799.

Hawthorne, F.C., and Ferguson, R.B. (1975) Refinement of crystal-structure of Krohnkite. Acta Crystallographica Section B-Structural Science, 31, 1753-1755.

Hug, S.J. (1997) In situ Fourier Transform Infrared measurements of sulfate adsorption on hematite in aqueous solutions. Journal of Colloid and Interface Science, 188, 415-422.

Kitahama, K., Kiriyama, R., and Baba, Y. (1975) Refinement of crystal-structure of scorodite. Acta Crystallographica Section B-Structural Science, 31, 322-324.

López-Archilla, A.I., Marin, I., and Amils, R. (2001) Microbial community

composition and ecology of an acidic aquatic environment: The Tinto River, Spain. Microbial Ecology, 41, 20-35.

Lane, M.D. (2007) Mid-infrared emission spectroscopy of sulfate and sulfate-bearing minerals. American Mineralogist, 92, 1-18.

Langmuir, D., Mahoney, J., and Rowson, J. (2006) Solubility products of amorphous ferric arsenate and crystalline scorodite ($FeAsO_4 \cdot 2H_2O$) and their application to arsenic behavior in buried mine tailings. Geochimica Et Cosmochimica Acta, 70, 2942-2956.

Le Berre, J.F., Gauvin, R., and Demopoulos, G.P. (2008) A study of the crystallization kinetics of scorodite via the transformation of poorly crystalline ferric arsenate in weakly acidic solution. Colloids and Surfaces A: Physicochemical and Engineering Aspects, 315, 117-129.

Ma, X., Gomez, M.A., Yuan, Z.D., Zhang, G.Q., Wang, S.F., Li, S.F., Yao, S.H., Wang, X., and Jia, Y.F. (2019) A novel method for preparing an As(V) solution for scorodite synthesis from an arsenic sulphide residue in a Pb refinery. Hydrometallurgy, 183, 1-8.

Ma, X., Yuan, Z.D., Gomez, M.A., Wang, X., Wang, S.F., Yao, S.H., and Jia, Y.F. (2017) A qualitative and quantitative investigation of partitioning and local structure of arsenate in barite lattice during coprecipitation of barium, sulfate, and arsenate. American Mineralogist, 102, 2512-2520.

Maillot, F., Morin, G., Juillot, F., Bruneel, O., Casiot, C., Ona-Nguema, G., Wang, Y.H., Lebrun, S., Aubry, E., and Vlaic, G. (2013) Structure and reactivity of As(III)- and

As(V)-rich schwertmannites and amorphous ferric arsenate sulfate from the Carnoulès acid mine drainage, France: Comparison with biotic and abiotic model compounds and implications for As remediation. Geochimica Et Cosmochimica Acta, 104, 310-329.

Majzlan, J., and Myneni, S.C.B. (2005) Speciation of iron and sulfate in acid waters: Aqueous clusters to mineral precipitates. Environmental Science & Technology, 39, 188-194.

Morin, G., Juillot, F., Casiot, C., Bruneel, O., Personne, J.C., Elbaz-Poulichet, F., Leblanc, M., Ildefonse, P., and Calas, G. (2003) Bacterial formation of tooeleite and mixed arsenic(III) or arsenic(V)-iron(III) gels in the carnoulbs acid mine drainage, France. A XANES, XRD, and SEM study. Environmental Science & Technology, 37, 1705-1712.

Min, X.B., Liao, Y.P., Chai, L.Y., Yang, Z.H., Xiong, S., Liu, L. and Li, Q.Z. (2015). Removal and stabilization of arsenic from anode slime by forming crystal scorodite. Trans. Nonferrous Met. Soc. China, 25(4): 1298-1306.

Murciego, A., Álvarez-Ayuso, E., Pellitero, E., Rodríguez, M.a., García-Sánchez, A., Tamayo, A., Rubio, J., Rubio, F., and Rubin, J. (2011) Study of arsenopyrite weathering products in mine wastes from abandoned tungsten and tin exploitations. Journal of Hazardous Materials, 186, 590-601.

Myneni, S.C.B. (2000) X-Ray and vibrational spectroscopy of sulfate in earth materials. Reviews in Mineralogy & Geochemistry, 40, 113-172.

Myneni, S.C.B., Traina, S.J., Waychunas, G.A., and Logan, T.J. (1998) Vibrational

589 spectroscopy of functional group chemistry and arsenate coordination in ettringite.
590 Geochimica Et Cosmochimica Acta, 62, 3499-3514.
591 Nordstrom, D.K., Alpers, C.N., Ptacek, C.J., and Blowes, D.W. (2000) Negative pH
592 and extremely acidic mine waters from Iron Mountain, California. Environmental
593 Science & Technology, 34, 254-258.
594 Okude, N., Nagoshi, M., Noro, H., Baba, Y., Yamamoto, H., and Sasaki, T.A. (1999) P
595 and S K-edge XANES of transition-metal phosphates and sulfates. Journal of
596 Electron Spectroscopy and Related Phenomena, 101–103, 607-610.
597 Omori, K. (1968) Infrared diffraction and the far infrared spectra of anhydrous sulfates.
598 Mineralogical Journal, 5, 334-354.
599 Paktunc, D., and Bruggeman, K. (2010) Solubility of nanocrystalline scorodite and
600 amorphous ferric arsenate: Implications for stabilization of arsenic in mine wastes.
601 Applied Geochemistry, 25, 674-683.
602 Paktunc, D., and Dutrizac, J.E. (2003) Characterization of arsenate-for-sulfate
603 substitution in synthetic jarosite using X-ray diffraction and X-ray absorption
604 spectroscopy. Canadian Mineralogist, 41, 905-919
605 Peak, D., Ford, R.G., and Sparks, D.L. (1999) An in situ ATR-FTIR investigation of
606 sulfate bonding mechanisms on goethite. Journal of Colloid and Interface Science,
607 218, 289-299.
608 Powers, D.A., Rossman, G.R., Schugar, H.J., and Gray, H.B. (1975) Magnetic behavior
609 and infrared spectra of jarosite, basic iron sulfate, and their chromate analogs.
610 Journal of Solid State Chemistry, 13, 1-13.

Qi, X.J., Li, Y.K., Wei, L.H., Hao, F.Y., Zhu, X., Wei, Y.G., Li, K.Z., and Wang, H. (2020) Disposal of high-arsenic waste acid by the stepwise formation of gypsum and scorodite. RSC Advances, 10, 29-42.

Sörbo, B. (1987) Sulfate: Turbidimetric and nephelometric methods. Methods in Enzymology, 143, 3-6.

Singhania, S., Wang, Q.K., Filippou, D., and Demopoulos, G.P. (2006) Acidity, valency and third-ion effects on the precipitation of scorodite from mixed sulfate solutions under atmospheric-pressure conditions. Metallurgical and Materials Transactions B-Process Metallurgy and Materials Processing Science, 37, 189-197.

Ventruti, G., Della Ventura, G., Gomez, M.A., Capitani, G., Sbroscia, M., and Sodo, A. (2020) High-temperature study of basic ferric sulfate, $FeOHSO_4$. Physics and Chemistry of Minerals, 47.

Wang, S.F., Ma, X., Zhang, G.Q., Jia, Y.F., and Hatada, K. (2016) New insight into the local structure of hydrous ferric arsenate using full-potential multiple scattering analysis, density functional theory calculations, and vibrational spectroscopy. Environmental Science & Technology, 50, 12114-12121.

Yang, J.Q., Chai, L.Y., Yue, M.Q., and Li, Q.Z. (2015) Complexation of arsenate with ferric ion in aqueous solutions. RSC Advances, 5, 103936-103942.

Zhu, X., Kirk Nordstrom, D., Blaine McCleskey, R., Wang, R., Lu, X., Li, S., and Henry Teng, H. (2019) On the thermodynamics and kinetics of scorodite dissolution. Geochimica et Cosmochimica Acta, 265, 468-477.

LIST OF FIGURE CAPTIONS

FIGURE 1. Optical images of the Natural-scorodite. The red and green dot represent the scorodite and pyrite crystal, respectively.

FIGURE 2. Contents of SO_4^{2-} in scorodite as a function of initial Na^+ concentrations at pH 1.2 and 1.8.

FIGURE 3. Comparison of XRD patterns of Natural-scorodite, SO_4-ferric arsenate, scorodite with SO_4-scorodite formed at pH 1.2 and various initial Na^+ concentrations.

FIGURE 4. SEM images, elemental mapping, and EDX results of SO_4-scorodite formed at pH 1.2 in the absence of Na^+ (**a**) and in the presence of 1 M (**b**), 2 M(**c**), and 4 M (**d**) Na^+.

FIGURE 5. SEM, elemental cross sectional mapping images of (**a**) Natural-scorodite and SO_4-scorodite formed at pH 1.2 in the absence of Na^+ and in the presence of 1 M (**b**) and 4 M **(c)** Na^+. The dotted lines represent the crosss section of the SO_4-scorodite.

FIGURE 6. FTIR spectra of Natural scorodite, reference compounds and SO_4-scorodite formed at various pH values and Na^+ concentrations. (**a**) 400 - 1300 and 2000 - 4000 cm^{-1} (**b**) 950 - 1300 cm^{-1} in SO_4-ferric arsenate, scorodite, and SO_4-scorodite.

FIGURE 7. Sulfur *K*-edge XANES spectra of (**a**) SO_4-scorodite (1 M Na^+ and pH 1.2), SO_4-ferric arsenate, Na_2SO_4, and (**b**) the pre-edge features in the S *K*-edge spectra of römerite, paracoquimbite, jarosite, and SO_4-scorodite. The continuous energy region above the adsorption edge was magnified from 2490 - 2510 eV in (**a**). A, B, and C represent pre-edge feature, white line peak and $1s \rightarrow$ continuum-state transition,

653 respectively.

654 **FIGURE 8.** DFT optimized (**a**) unit cell of SO_4-scorodite and (**b**) SO_4^{2-} local

655 coordination environments in SO_4-scorodite.

656 **FIGURE 9.** Sulfur (S) *K*-edge k^3-weighted χ functions (**a**), Fourier transformed (FTs)χ

657 functions (**b**), and real part of Fourier transformed EXAFS spectra (**c**) of reference

658 compounds (Na_2SO_4 and paracoquimbite) and SO_4-scorodite (1 M Na^+ and pH 1.2).

TABLES

TABLE 1. Comparison of S-O vibration band positions of reference compounds with SO_4-scorodite in the FTIR spectra.

Mineral	Symmetry	S-O Stretching vibrations (cm^{-1})			
		v_1	v_2	v_3	v_4
Na_2SO_4	C_1			1132 (shoulder)	615/640
römerite	C_{3v}	987		1101/1151	615
paracoquimbite	C_{2v}	1024		1054/110/1195	
jarosite	C_v	1006	445	1220/1197	635
$FeOHSO_4$ [(a)]	C_1	1058		1172/1138/1112	638/650
SO_4-scorodite	C_1	1001		1070/1103/1205	

(a): The FTIR data was reported by Powers et al. (1975).

TABLE 2. The DFT calculated interatomic distances of S-O, S-Fe in SO_4-scorodite and the reported interatomic distances of S-O, S-Fe in $FeOHSO_4$, and As-O, As-Fe in scorodite.

Sample Formula	Description	Bond length (Å)	
		S-O, CN = 4	S-Fe, CN = 4
SO_4-scorodite	one SO_4^{2-} substituting for one AsO_4^{3-}	1.46; 1.48	3.29; 3.29;
$Fe_8(AsO_4)_7SO_4(OH)\cdot 15H_2O$		1.48; 1.46	3.33; 3.41
$FeOHSO_4$ (a)	determined by XRD	1.44; 1.44	3.30; 3.31
$Fe_{15}(OH)_{15}(SO_4)_{15}$		1.46; 1.46	3.30; 3.31
$Fe_2(SO_4)_3$ (b)	determined by XRD	1.46; 1.47	3.23; 3.26
$Fe_{26}S_{30}O_{166}$		1.47; 1.47	3.29; 3.36
		As-O, CN = 4	**As-Fe, CN = 4**
Scorodite (c)	unit cell determined by XRD[b]	1.67; 1.68	3.34; 3.35
$Fe_8(AsO_4)_8\cdot 16H_2O$		1.68; 1.69	3.36; 3.39

(a): Ventruti et al. 2005.
(b): Christidis and Rentzeperis 1976.
(c): Kitahama et al. 1975.

TABLE 3. The shell-fit results for the S *K*-edge EXAFS of reference compounds ($NaSO_4$ and paracoquimbite) and SO_4-scorodite. CN: coordination number. R_{apt}: interatomic distance. Σ^2: Debye-Waller parameter. ΔE: energy-shift parameter. χ^2_{red}: reduced chi-square. *R*-factor: mean-square misfit between the measured and the modeled data. The number of independent points (N_{idp}) and variables (N_{var}) were 11.95 and 6, respectively.

Path	CN	R_{path} (Å)	σ^2 (Å^2)×10^{-2}	ΔE (eV)	χ^2_{red}	*R*-factor
Na_2SO_4						
S-O	4	1.45(4)	0.059(4)	2.20(6.9)	105	0.022
Paracoquimbite						
S-O	4	1.46(2)	0.154(11)	0.50(5.1)	218	0.028
S-O-O	12	2.76(7)	0.190(11)	0.50(5.1)		
S-Fe	2	3.23(5)	0.820(11)	0.50(5.1)		
SO_4-scorodite ($Fe_2(SO_4)_3$ as the initial model)						
S-O	4	1.47(1)	0.019(42)	7.60(2.38)	28	0.016
S-O-O	12	2.71(2)	0.032(42)	7.60(2.38)		
S-Fe	4	3.33(3)	0.986(42)	7.60(2.38)		
SO_4-scorodite (DFT optimized structure as the initial model)						
S-O	4	1.47(1)	0.031(45)	7.10(2.56)	32	0.021
S-O-O	12	2.86(2)	0.053(45)	7.10(2.56)		
S-Fe	4	3.31(2)	1.001(34)	7.10(2.56)		

Figure 1

Scorodite crystal

Pyrite crystal

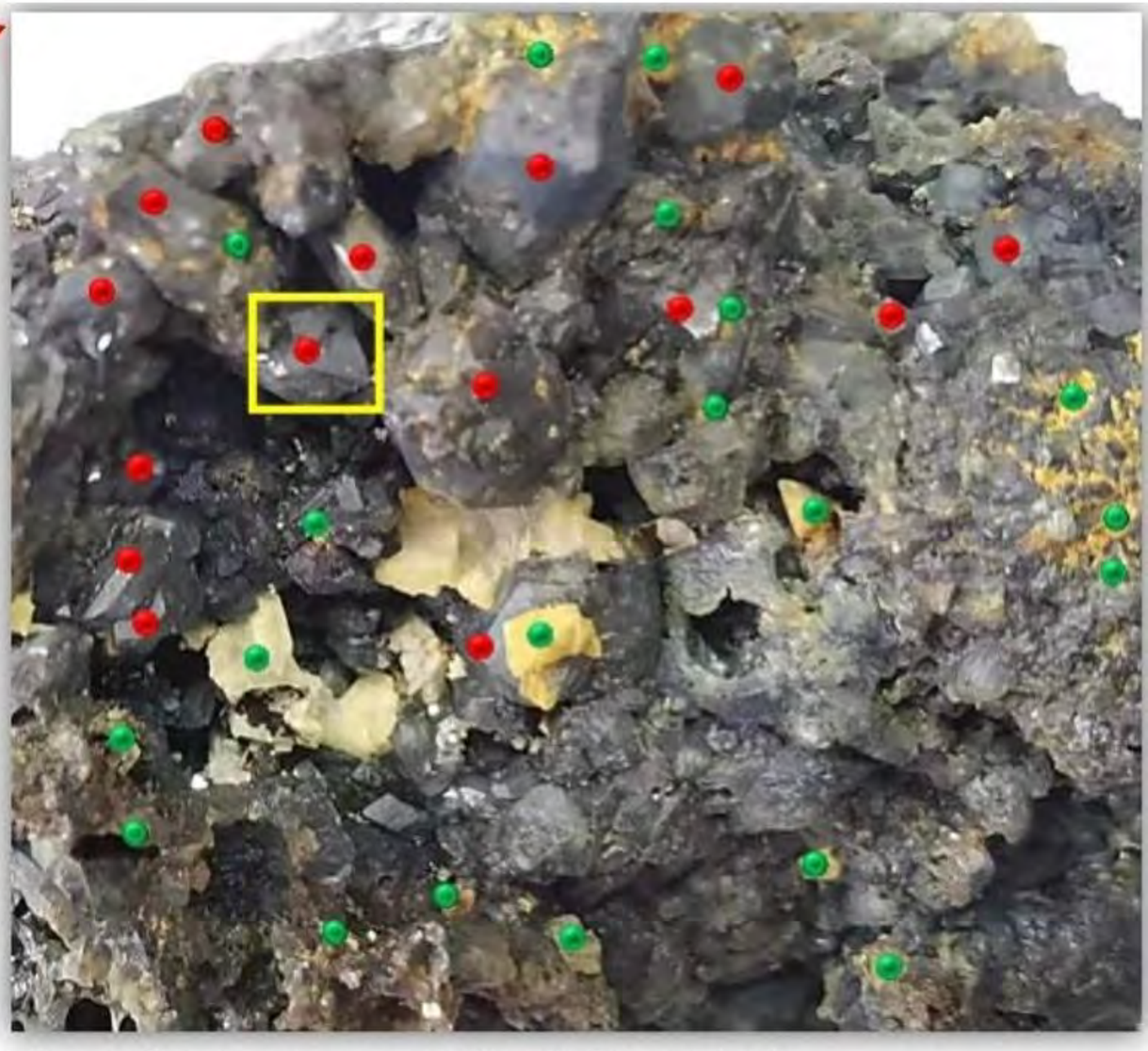

The yellow part was cut for SEM analysis

Figure 2

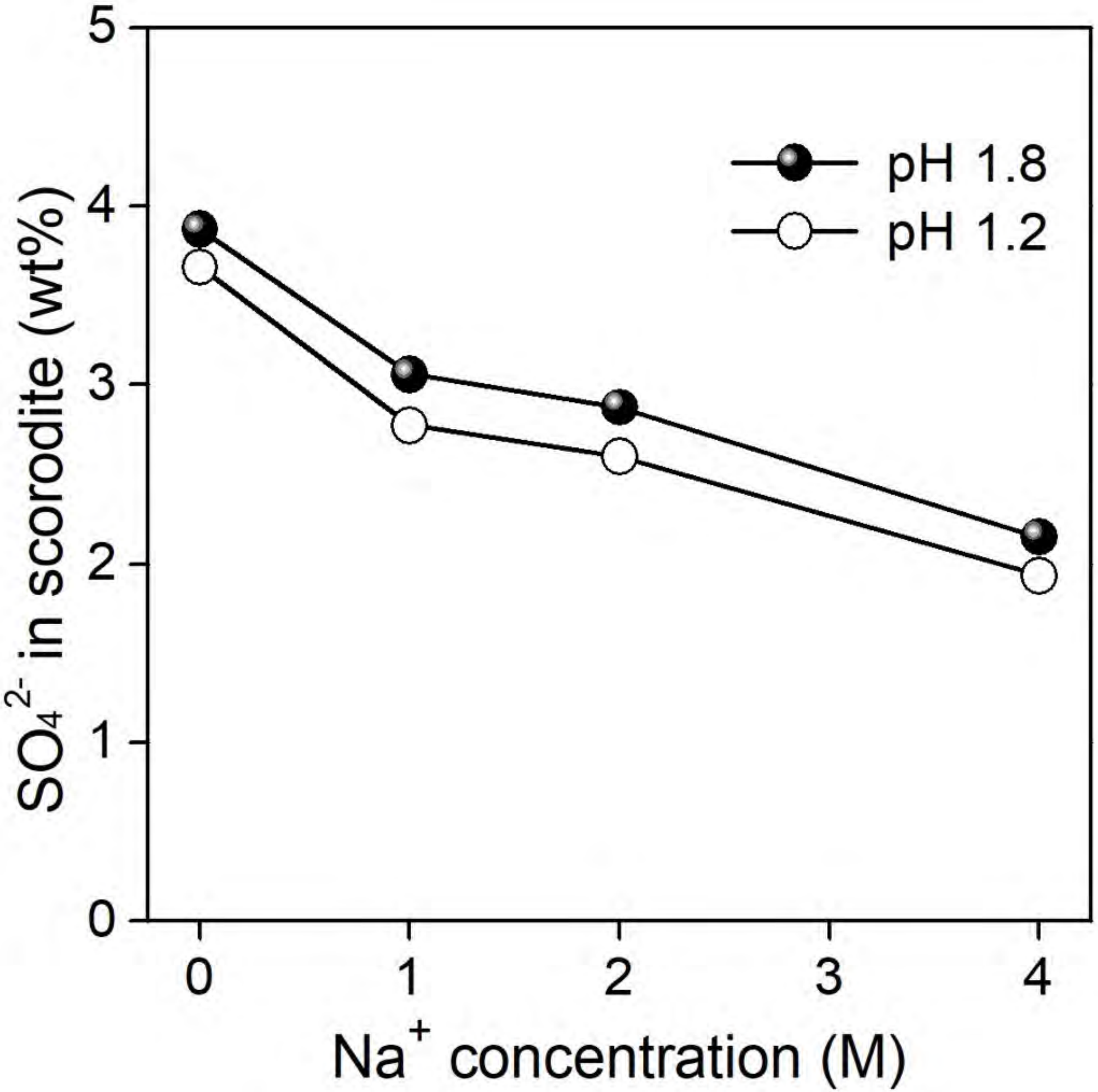
pH 1.8
pH 1.2
SO_4^{2-} in scorodite (wt%)
0
1
2
3
4
5
0
1
2
3
4
Na^+ concentration (M)

Figure 3

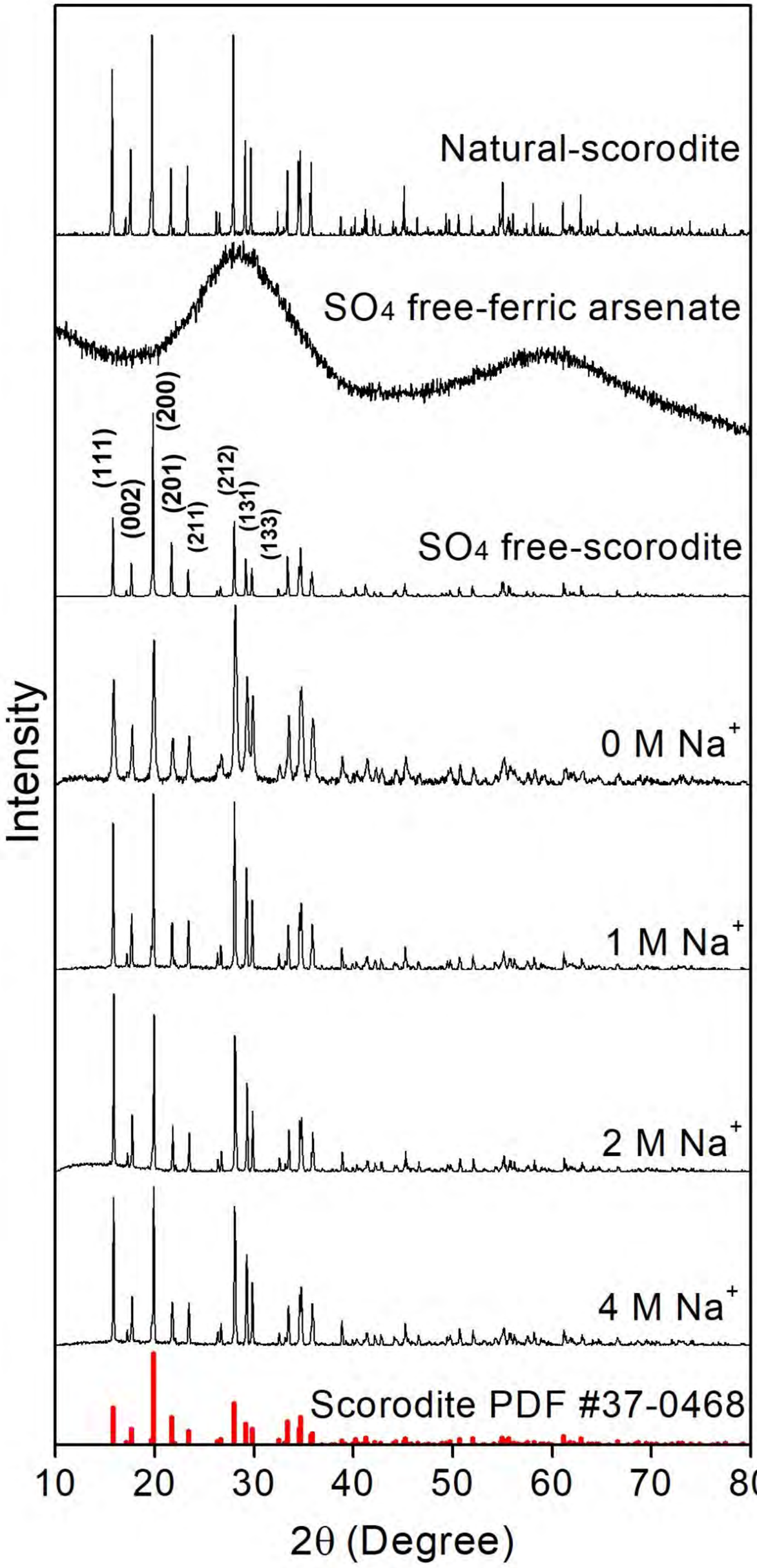
Natural-scorodite
SO4 free-ferric arsenate
(111)
(002)
(200)
(201)
(211)
(212)
(131)
(133)
SO4 free-scorodite
0 M Na+
1 M Na+
2 M Na+
4 M Na+
Scorodite PDF #37-0468
Intensity
10
20
30
40
50
60
70
80
2θ (Degree)

Figure 4

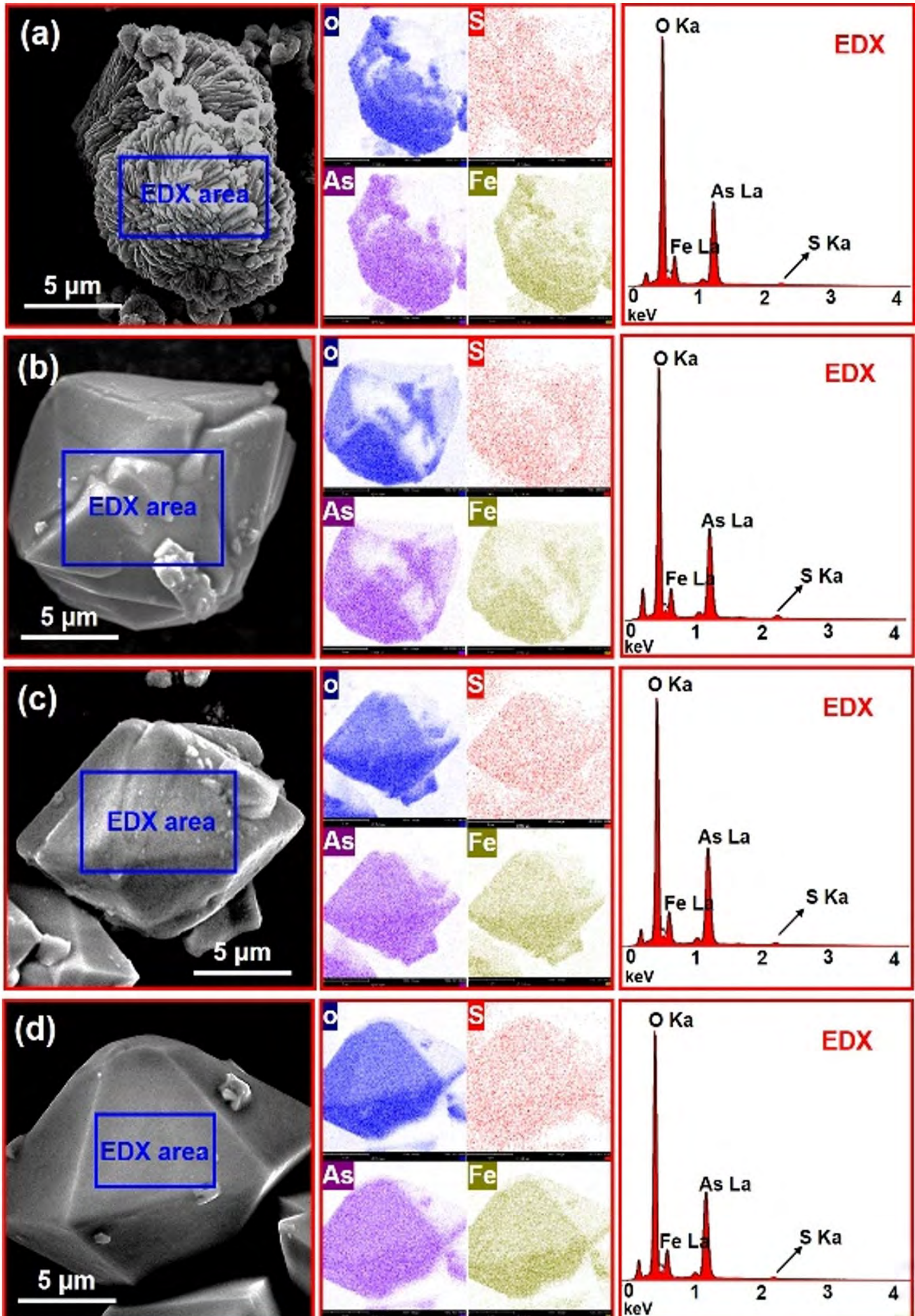
(a)
EDX area
5 μm
O
S
As
Fe
O Ka
EDX
As La
Fe La
S Ka
0
1
2
3
4
keV
(b)
EDX area
5 μm
O
S
As
Fe
O Ka
EDX
As La
Fe La
S Ka
0
1
2
3
4
keV
(c)
EDX area
5 μm
O
S
As
Fe
O Ka
EDX
As La
Fe La
S Ka
0
1
2
3
4
keV
(d)
EDX area
5 μm
O
S
As
Fe
O Ka
EDX
As La
Fe La
S Ka
0
1
2
3
4
keV

Figure 5

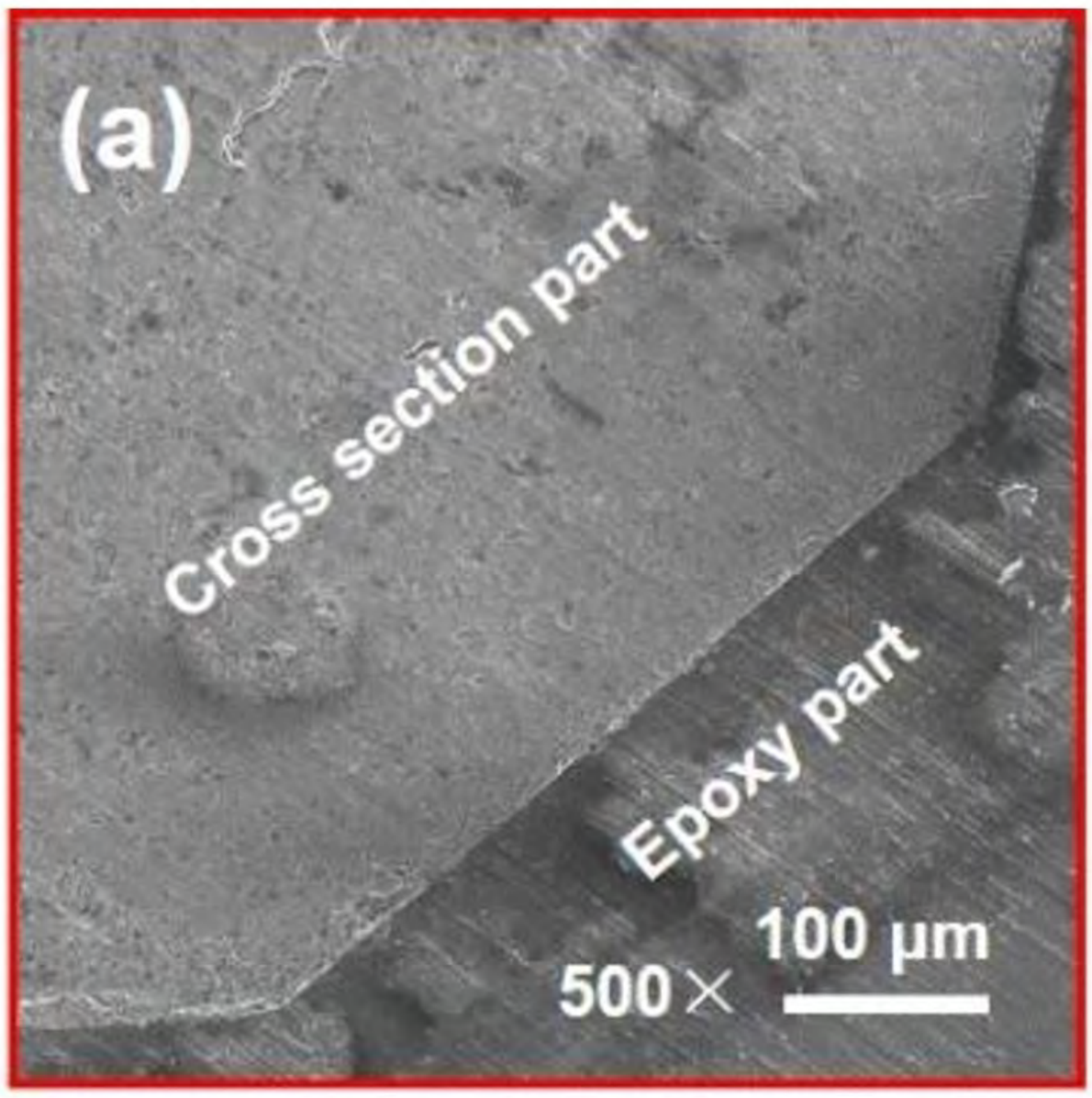
(a)
Cross section part
Epoxy part
500×
100 μm

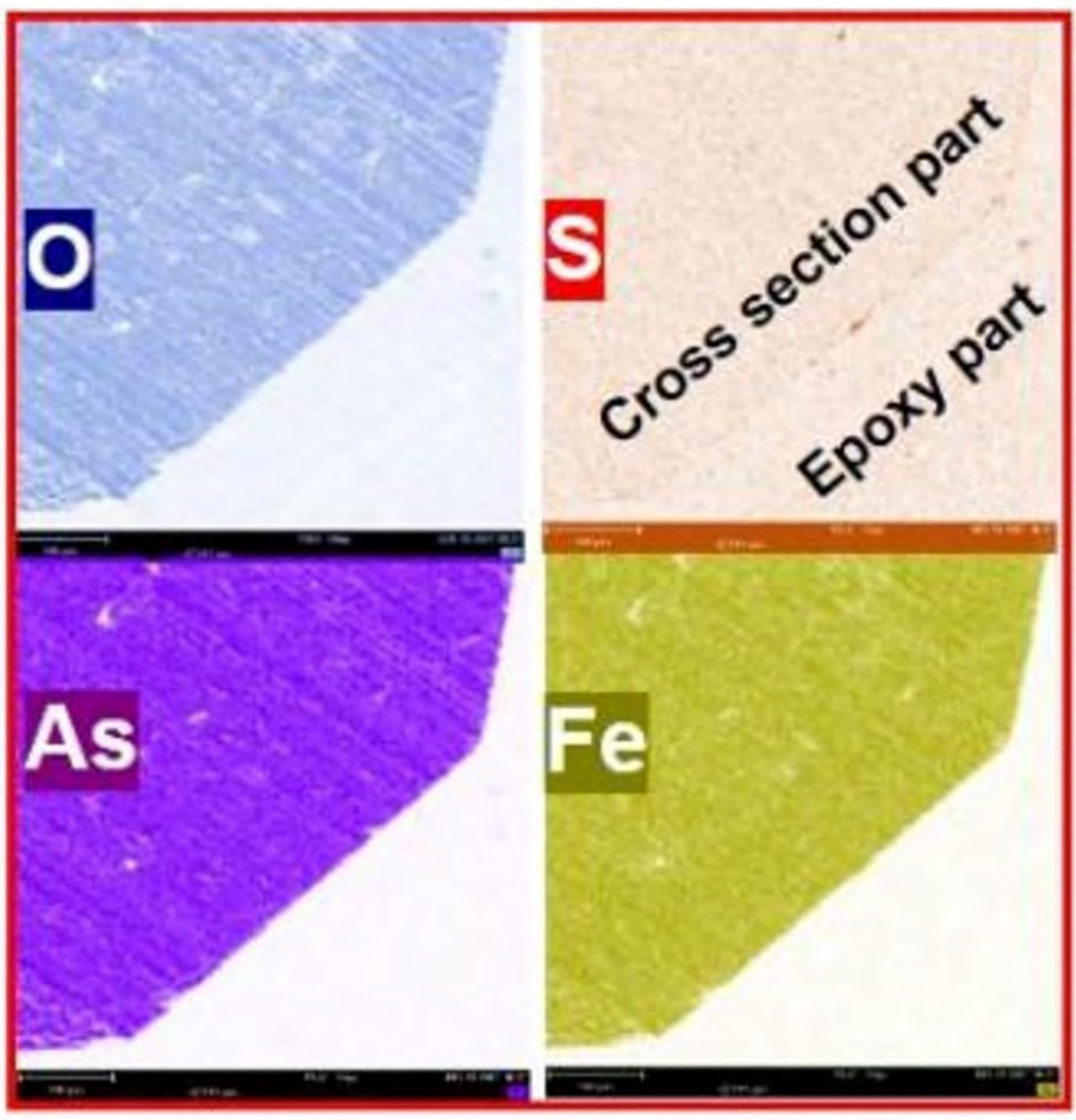
O
S
Cross section part
Epoxy part
As
Fe

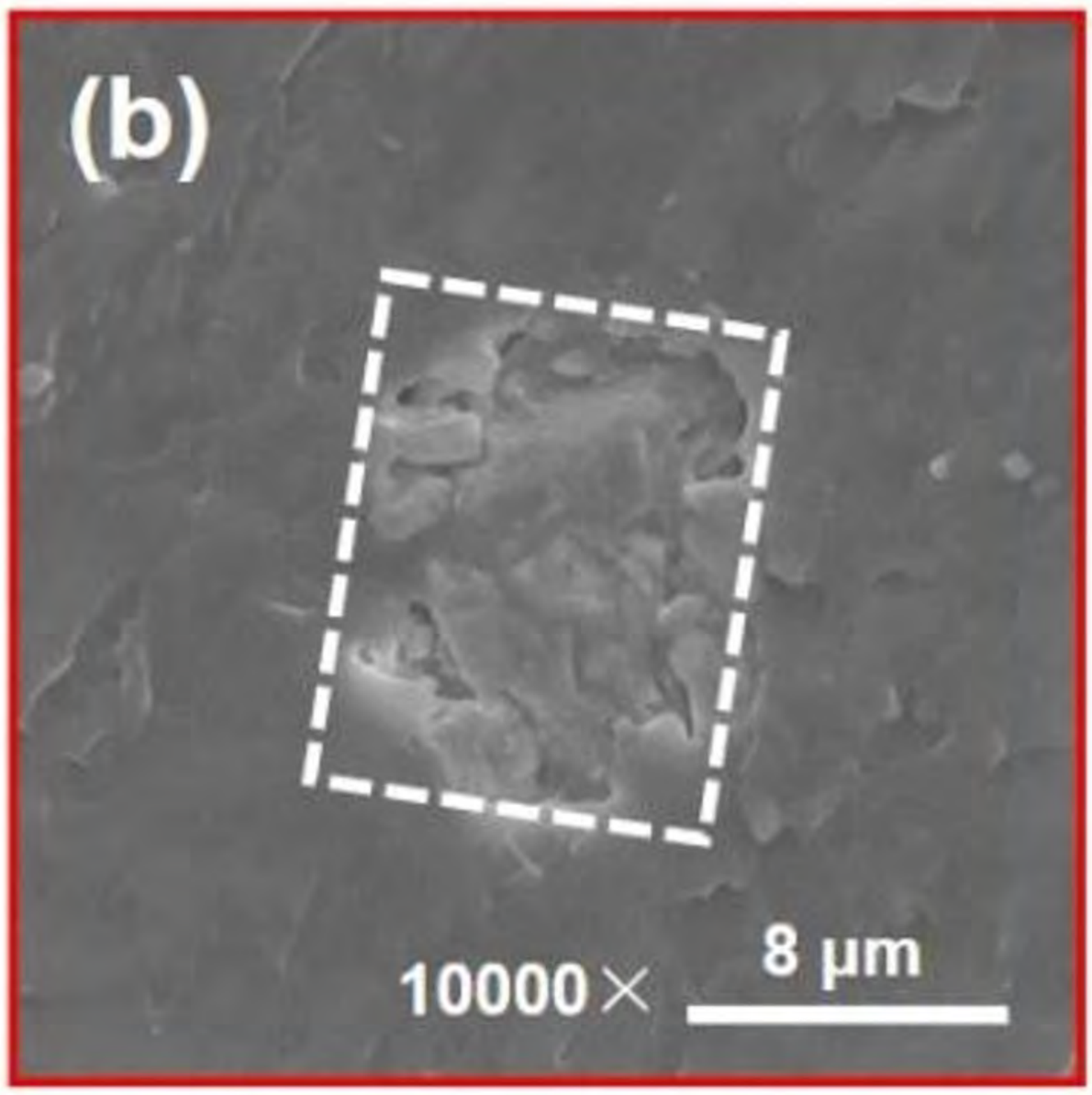
(b)
10000×
8 μm

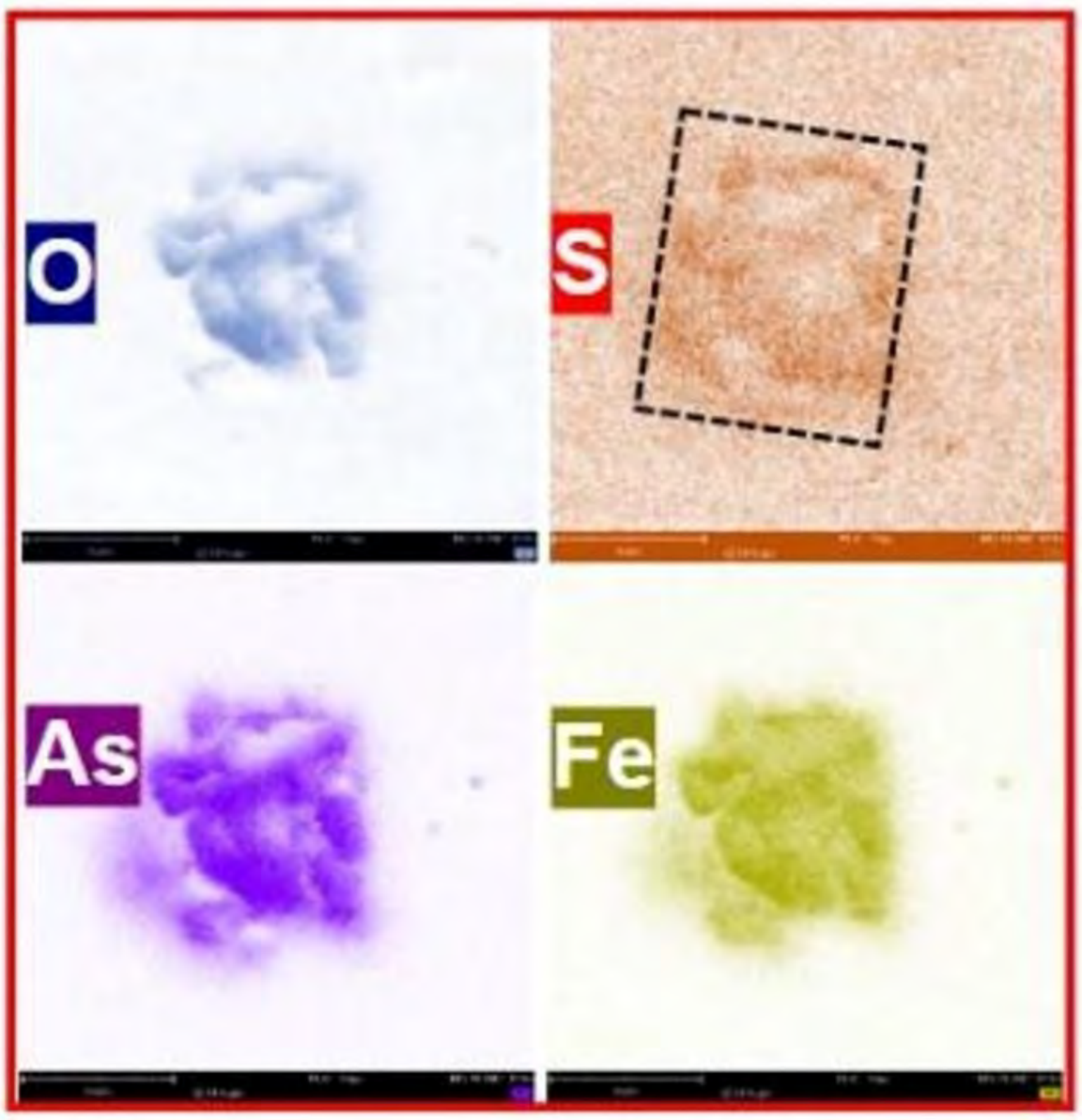
O
S
As
Fe

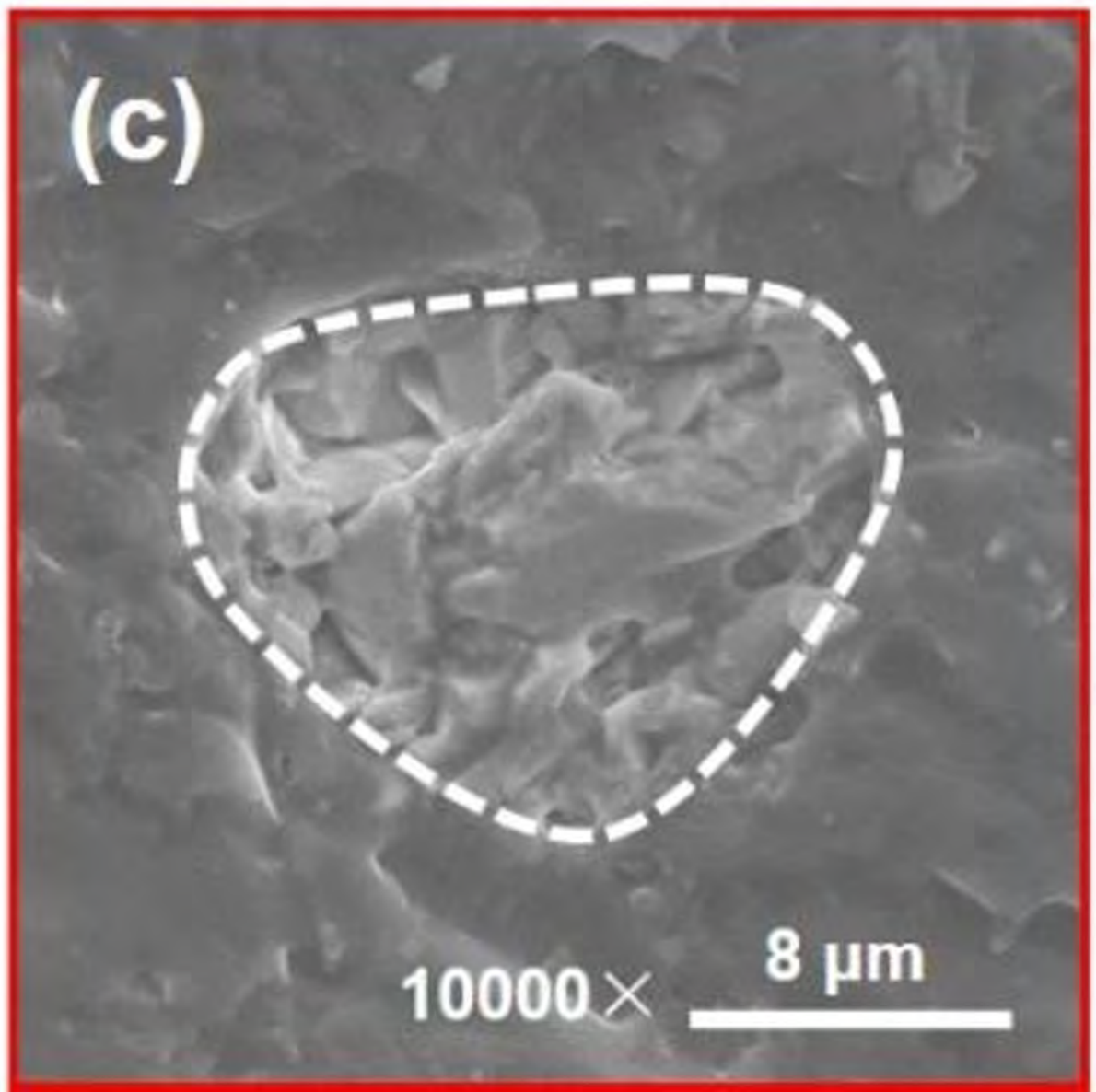
(c)
10000×
8 μm

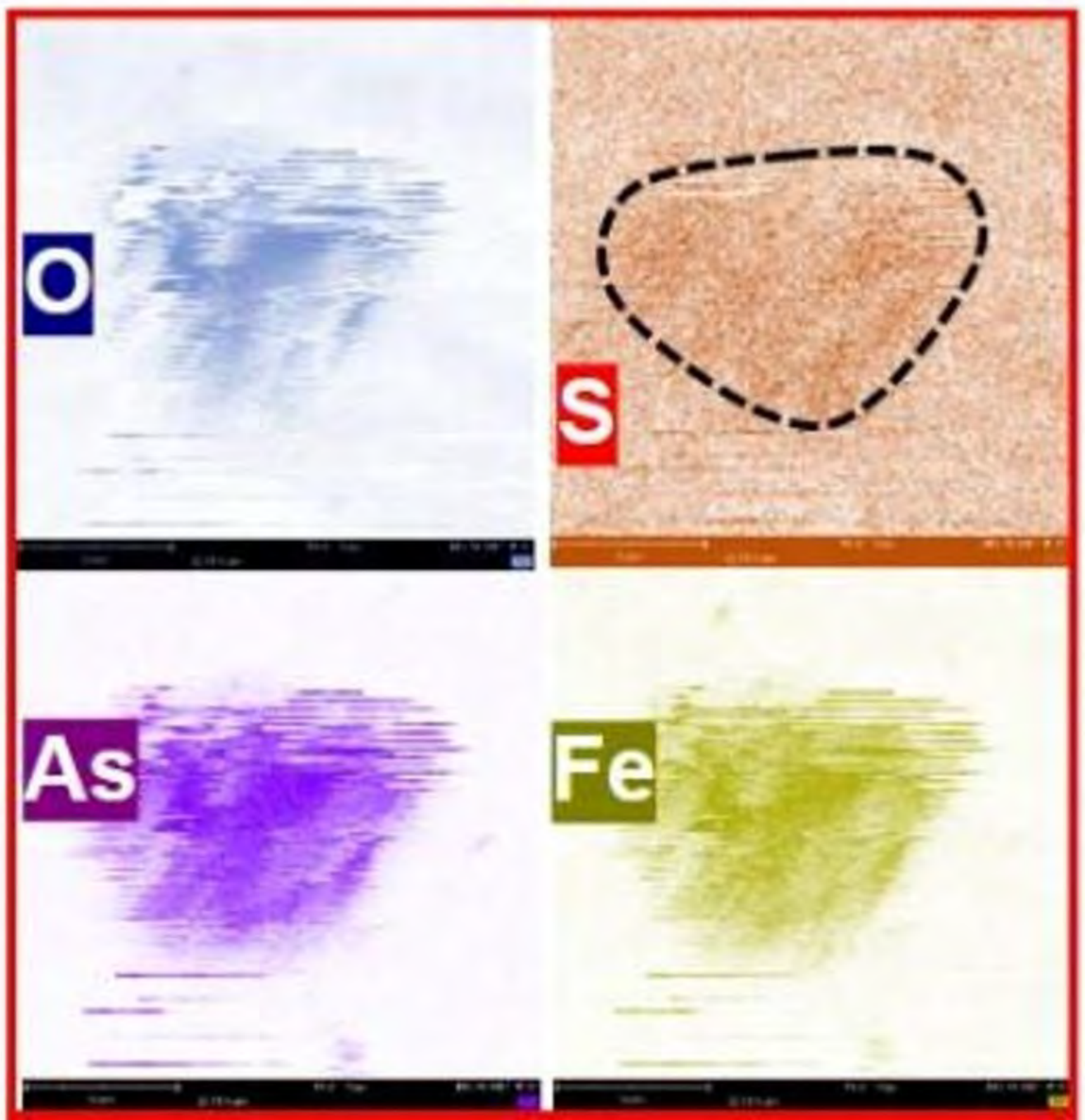
O
S
As
Fe

Figure 6

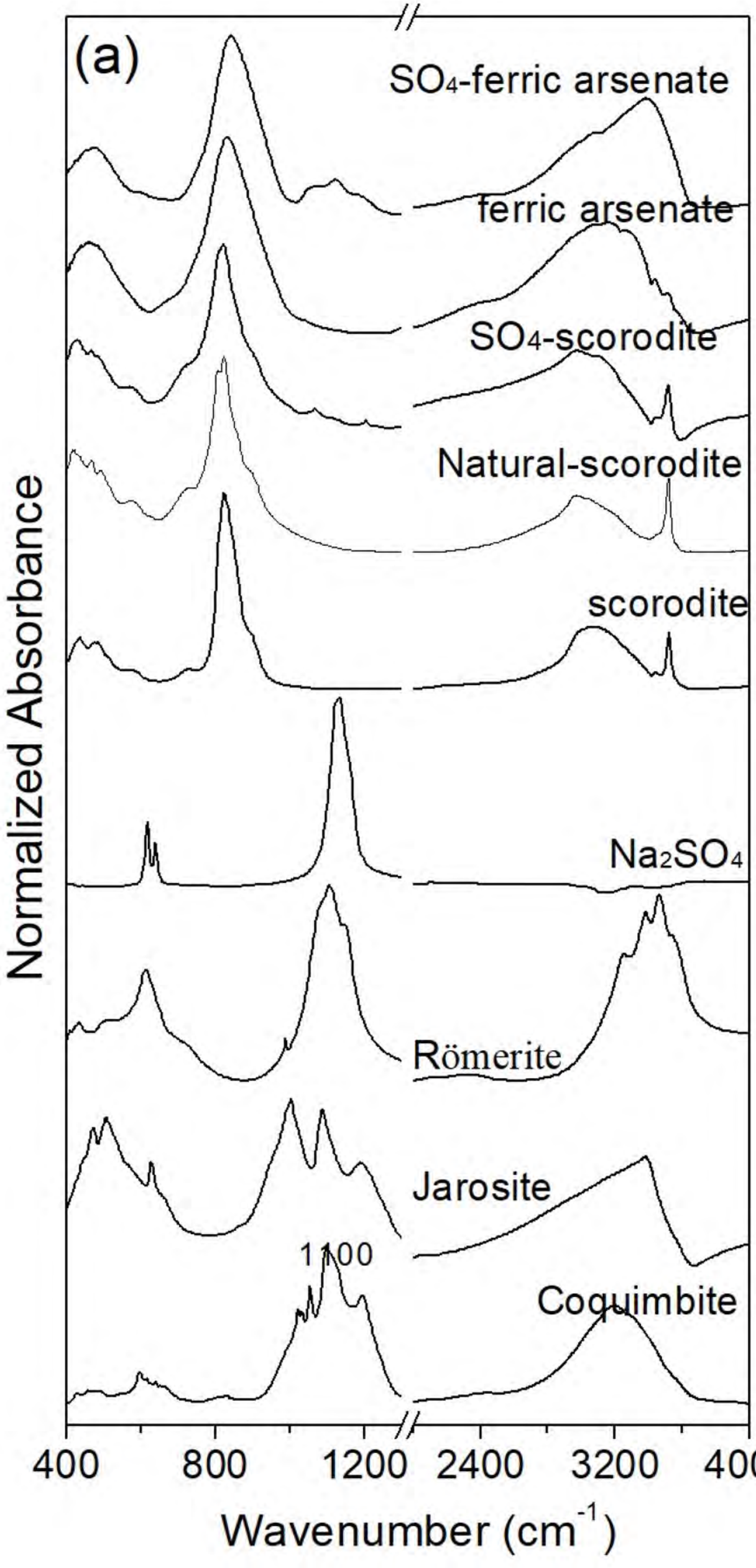
(a)
SO4-ferric arsenate
ferric arsenate
SO4-scorodite
Natural-scorodite
scorodite
Na2SO4
Römerite
Jarosite
1100
Coquimbite
Normalized Absorbance
400
800
1200
2400
3200
4000
Wavenumber (cm-1)

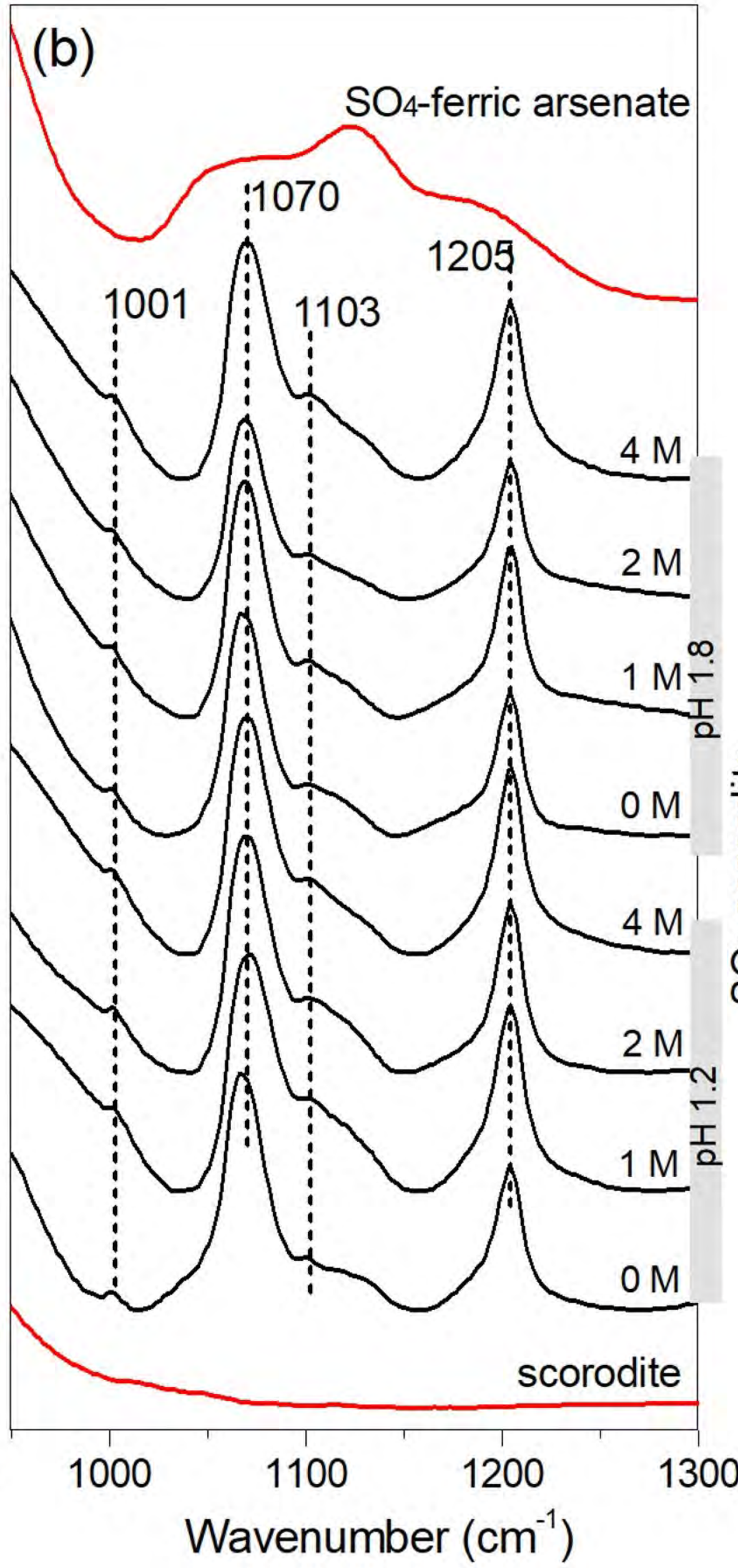
(b)
SO4-ferric arsenate
1070
1205
1001
1103
4 M
2 M
1 M
pH 1.8
0 M
4 M
2 M
1 M
pH 1.2
0 M
scorodite
SO4-scorodite
1000
1100
1200
1300
Wavenumber (cm-1)

Figure 7

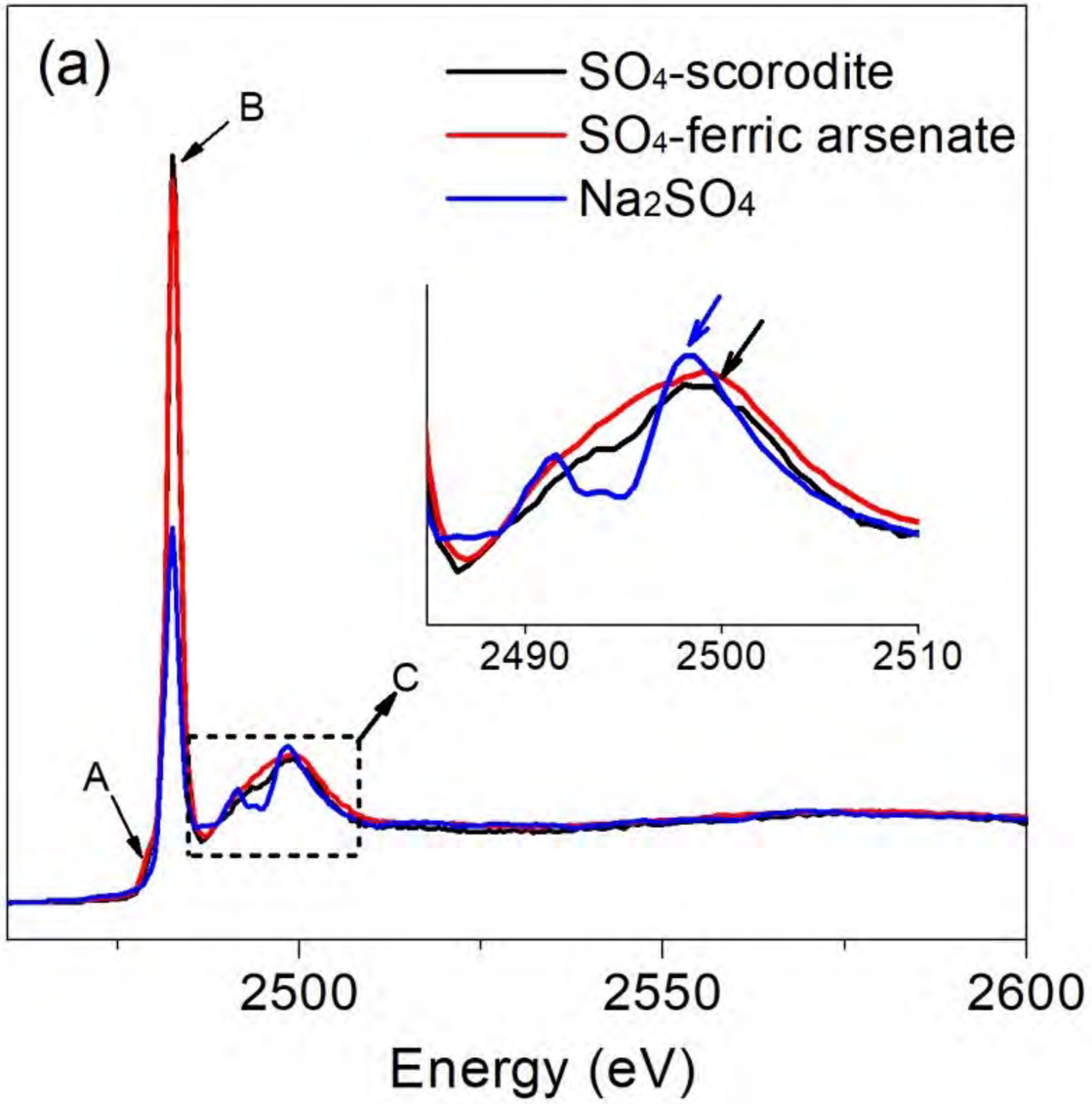
(a)
SO4-scorodite
SO4-ferric arsenate
Na2SO4
A
B
C
2490
2500
2510
2500
2550
2600
Energy (eV)

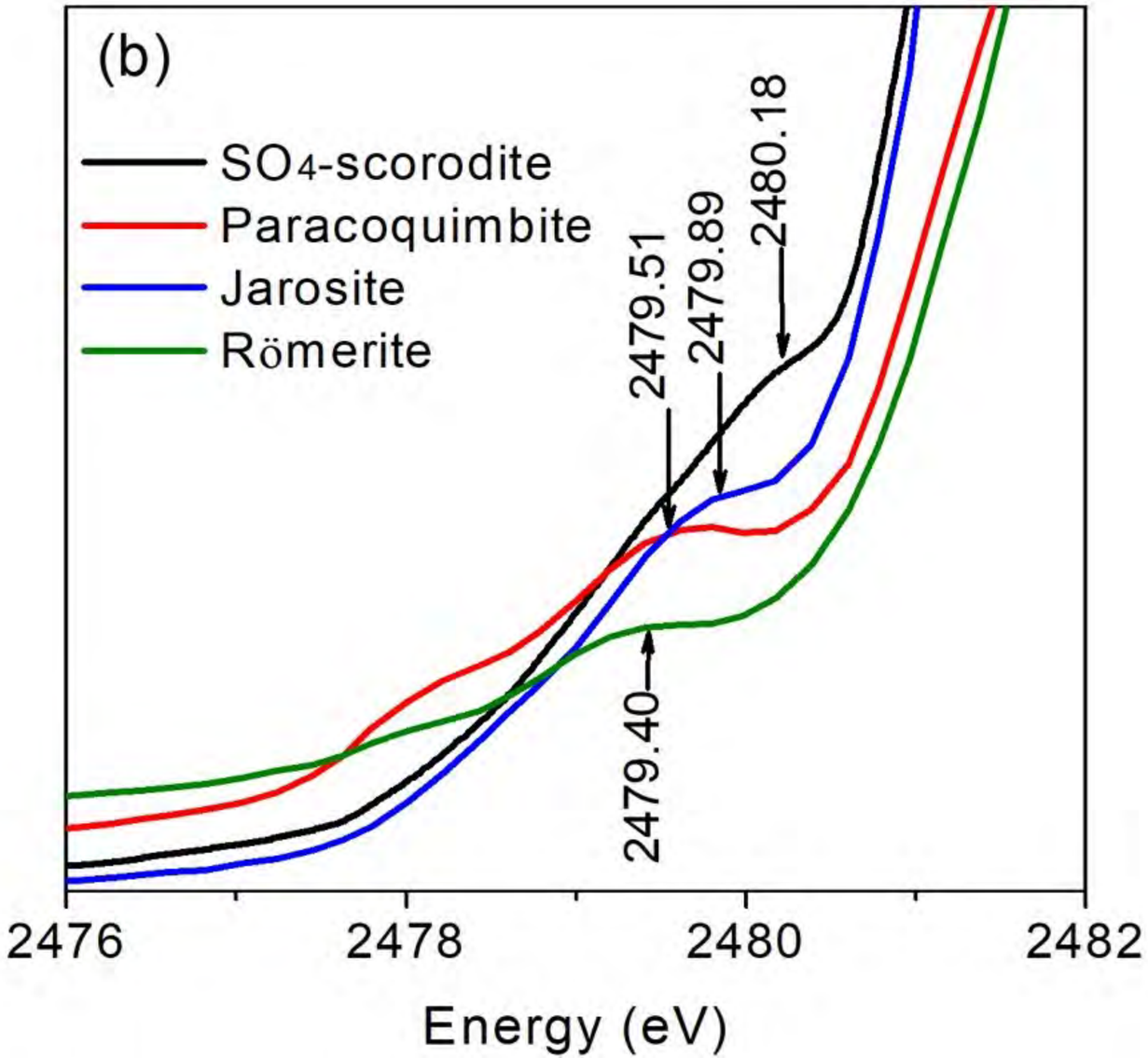
(b)
SO4-scorodite
Paracoquimbite
Jarosite
Römerite
2479.51
2479.89
2480.18
2479.40
2476
2478
2480
2482
Energy (eV)

Figure 8

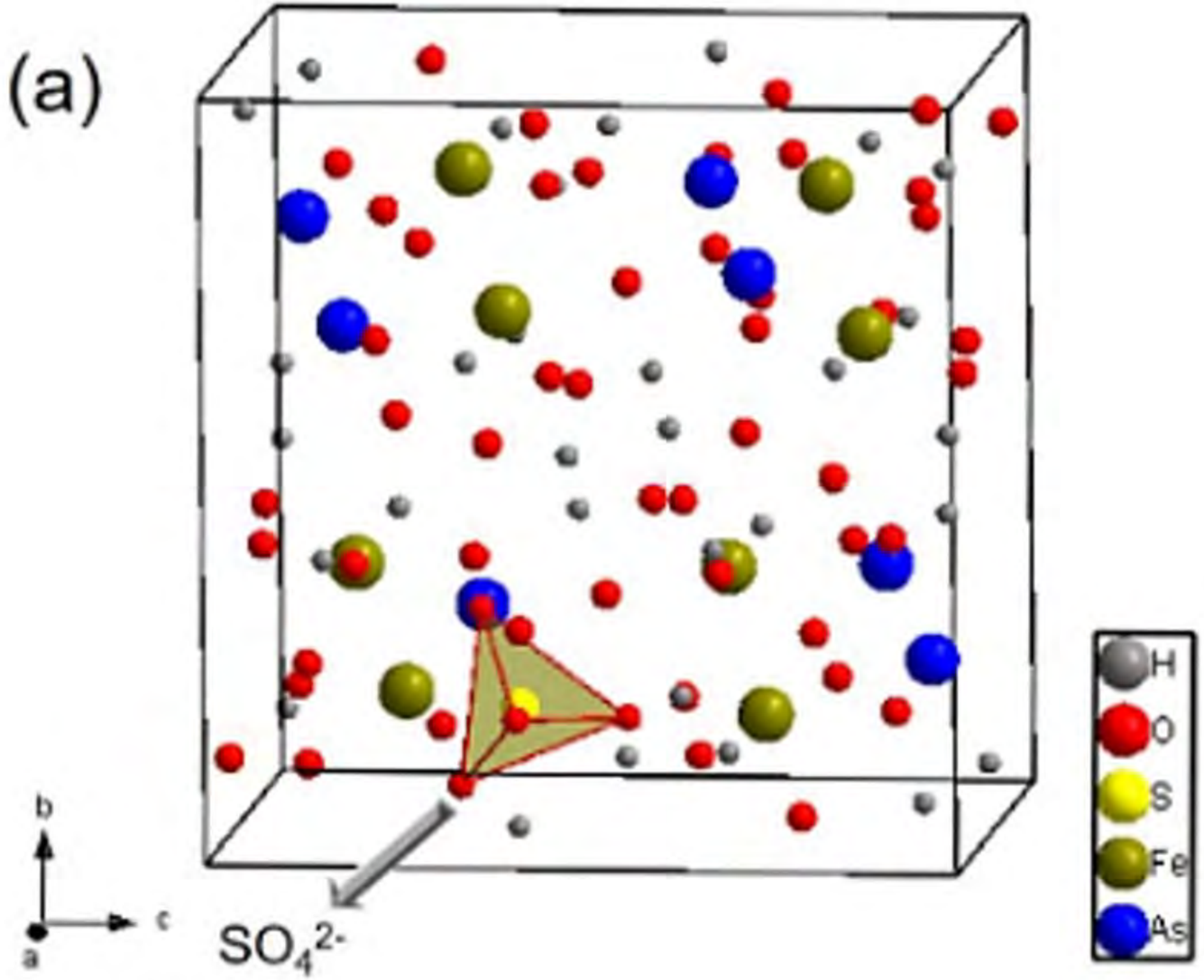

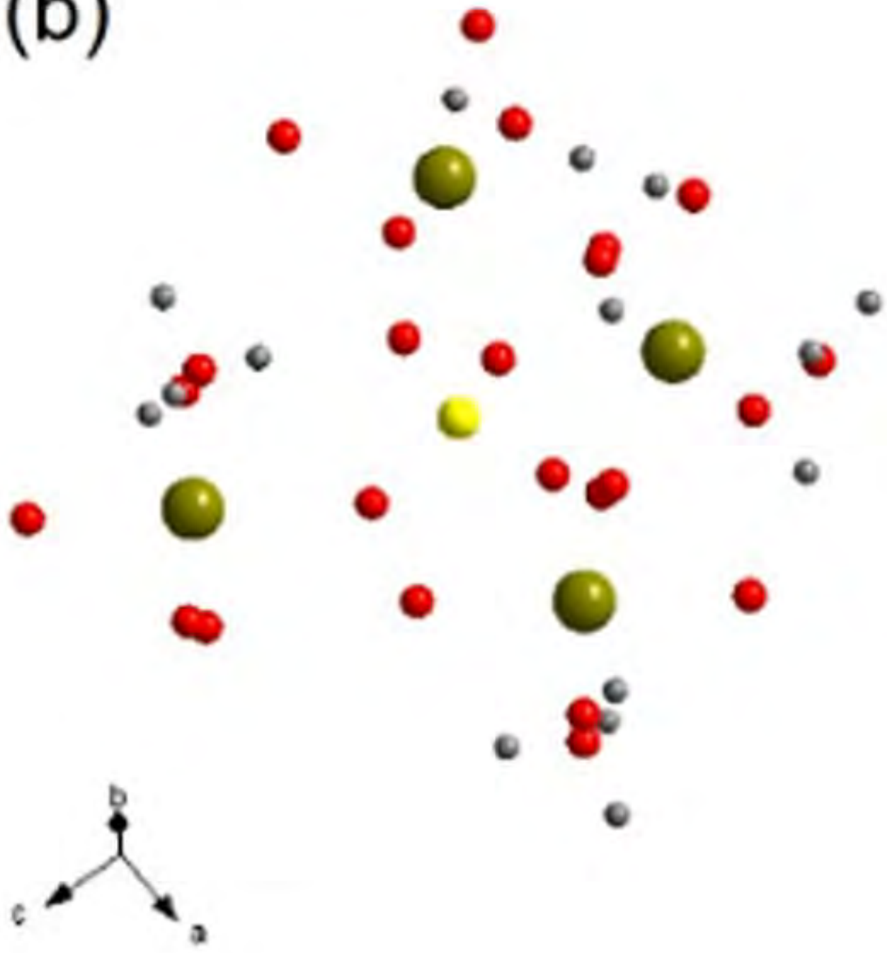

Figure 9

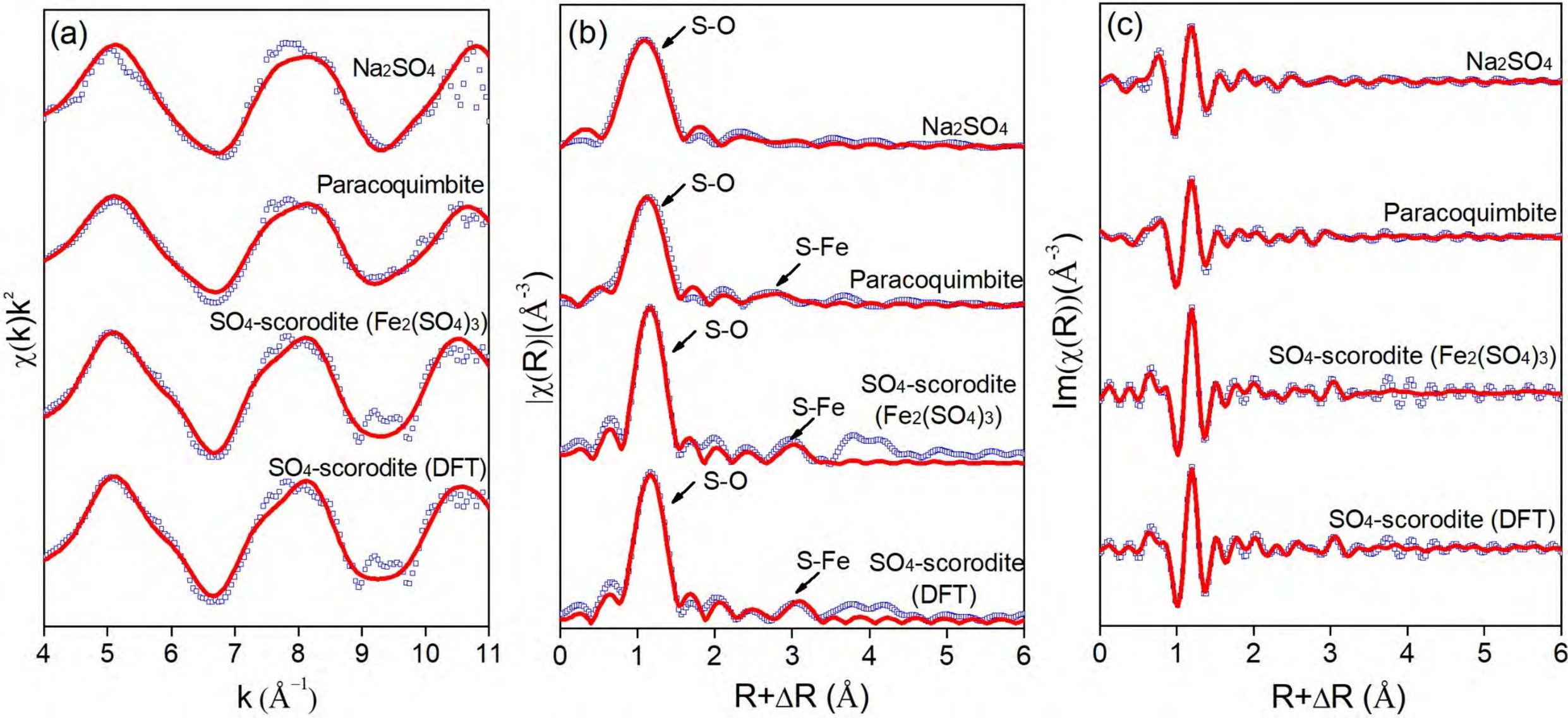
(a)
Na2SO4
Paracoquimbite
SO4-scorodite (Fe2(SO4)3)
SO4-scorodite (DFT)
χ(k)k²
k (Å⁻¹)
(b)
S-O
S-Fe
Na2SO4
Paracoquimbite
SO4-scorodite (Fe2(SO4)3)
SO4-scorodite (DFT)
|χ(R)|(Å⁻³)
R+ΔR (Å)
(c)
Na2SO4
Paracoquimbite
SO4-scorodite (Fe2(SO4)3)
SO4-scorodite (DFT)
Im(χ(R))(Å⁻³)
R+ΔR (Å)